



RESEARCH ARTICLE

10.1029/2022JD037003

Key Points:

- Convective gravity wave momentum flux (CGWMF) and drag (CGWD) are calculated using the Global Precipitation Measurement (GPM) and Modern-Era Retrospective Analysis for Research and Applications, Version 2 (MERRA-2) heating rate
- The CGWMF at the cloud top calculated using GPM is greater at high-phase speeds than that using MERRA-2 due to deeper clouds from GPM
- Using two different heating rates does not change significantly CGWD below $z = 40$ km in the tropics

Supporting Information:

Supporting Information may be found in the online version of this article.

Correspondence to:

H.-Y. Chun,
chunhy@yonsei.ac.kr

Citation:

Lee, H.-K., Kang, M.-J., Chun, H.-Y., Kim, D., & Shin, D.-B. (2022). Characteristics of latent heating rate from GPM and convective gravity wave momentum flux calculated using the GPM data. *Journal of Geophysical Research: Atmospheres*, 127, e2022JD037003. <https://doi.org/10.1029/2022JD037003>

Received 26 APR 2022
Accepted 29 AUG 2022

© 2022. The Authors.

This is an open access article under the terms of the [Creative Commons Attribution-NonCommercial-NoDerivs License](https://creativecommons.org/licenses/by-nc-nd/4.0/), which permits use and distribution in any medium, provided the original work is properly cited, the use is non-commercial and no modifications or adaptations are made.

Characteristics of Latent Heating Rate From GPM and Convective Gravity Wave Momentum Flux Calculated Using the GPM Data

Hyun-Kyu Lee¹ , Min-Jee Kang², Hye-Yeong Chun¹ , Donghyeck Kim¹ , and Dong-Bin Shin¹ 

¹Department of Atmospheric Sciences, Yonsei University, Seoul, Korea, ²School of Earth and Environmental Sciences, Seoul National University, Seoul, Korea

Abstract Parameterizations of convective gravity-wave (CGW) drag (CGWD) require cloud information as input parameters. As cloud information provided from reanalyses includes some uncertainties, observed cloud information is required for better representation of CGWs. For this, characteristics of the latent heating rate (LHR) based on the Global Precipitation Measurement (GPM) satellite over 6 yr (June 2014 to May 2020) are investigated, and the CGW momentum flux and CGWD based on an offline CGWD parameterization are calculated using the GPM-LHR and the Modern-Era Retrospective Analysis for Research and Applications, Version 2 (MERRA-2) background variables. Additionally, they are compared with those using LHR afforded by MERRA-2. The averaged cloud-bottom height is lower than that from MERRA but the cloud top height is similar for the both data, yielding deeper clouds from GPM that can generate more high phase-speed components of CGWs. The column-maximum heating rate, which is an input of the CGW momentum flux, of GPM-LHR is maximal near the equator and the secondary maximum locates in the winter hemisphere storm tracks. The maximum of the cloud top momentum flux (CTMF) of CGWs locates in the winter hemisphere storm tracks, with the GPM-CTMF being much larger than MERRA-CTMF, as extreme convective events occur more frequently in GPM. In the equatorial region above $z = 40$ km, the GPM-CGWD is significantly larger because high phase-speed components of CGWs that survive up to the upper stratosphere are abundant for GPM-CTMF, and this will contribute to drive more realistic semi-annual oscillation.

1. Introduction

Atmospheric gravity waves (GWs) influence large-scale flow due to the deposition of momentum and energy when they are dissipated (Lindzen, 1981). Convective gravity waves (CGWs) have a wide phase spectrum and thus can effectively transport momentum from the troposphere to the mesosphere. CGW forcing is an important driver of semi-annual oscillation (SAO) and quasi-biennial oscillation (QBO). Particularly, the impact of CGWs on QBO has been well appreciated, as small-scale CGWs provide approximately half of the eastward forcing in the eastward shear zone and most of the westward forcing in the westward shear zone (Ern et al., 2014; Holt et al., 2020; Kang et al., 2018; Kawatani et al., 2010; Y.-H. Kim & Chun, 2015a; Pahlavan et al., 2021).

GWs cannot be fully resolved in general circulation models due to the wide horizontal length scales ($\sim 1\text{--}1,000$ km), and thus, they must be parameterized in most GCMs (Y.-J. Kim et al., 2003). For decades, the parameterizations of the CGW drag (hereafter CGWD) have been developed by providing an analytic solution of internal GWs generated via diabatic forcing (Beres et al., 2004; Song & Chun, 2005). Choi and Chun (2011; CC11) modified the CGWD parameterization of Song and Chun (2005) by optimizing the propagation direction of the cloud top momentum flux (CTMF) and the moving speed of the diabatic source. Y.-H. Kim et al. (2013) showed that the representation of QBO was improved by including the CC11 parameterization in the Met Office Unified Model. Kang et al. (2017; hereafter, KCK17) proposed a CGWD parameterization including the nonlinearity effect of CGWs (Chun et al., 2008) to the CC11 parameterization.

When a CGWD parameterization is implemented into a GCM, the direct evaluation of the parameterization is not straightforward, because CGWD is merely a part of GCM, and whether the parameterization provides “right forcing” can only be confirmed by matching the model results with observations (KCK17; Plougonven et al., 2020). Therefore, the offline calculation of the CGWD parameterization using reanalysis data is necessary to evaluate the influence of the CGW parameterization. Kalisch et al. (2016) and Trinh et al. (2016) calculated CGW momentum flux (CGWMF) offline using the CC11 parameterization and found relatively good agreement

with that estimated from limb-sounding satellite observations. KCK17 and Kang et al. (2018) investigated the spatiotemporal variations in the CGWMF and drag using the offline parameterization of KCK17. They utilized Climate Forecast System Reanalysis (CFSR; Saha et al., 2010) data as input variables and set the magnitude of the momentum flux comparable to that of superpressure balloons (Jewtoukoff et al., 2013) to yield a realistic magnitude of CGWD. Due to the termination of the CFSR version 1, this offline approach was extended to Modern-Era Retrospective Analysis for Research and Applications, Version 2 (MERRA-2; Gelaro et al., 2017) data, which was used for estimating CGWD during the two recent QBO disruption periods (Kang & Chun, 2021; Kang et al., 2020).

Calculation of an offline CGWD parameterization requires the basic-state wind, temperature, cloud top and bottom heights, and latent heating rate (LHR) data. Among them, cloud information, such as cloud top and bottom heights and LHR, is not usually provided by most reanalyses, and even when it is occasionally provided, it is a purely model output without data assimilation. However, convective parameterizations in GCMs and reanalyses are well known for their uncertainties (Cui et al., 2017; Emori et al., 2005; Huaman & Schumacher, 2018; Jiang et al., 2011; J.-E. Kim & Alexander, 2013; Li et al., 2009; Lin et al., 2006; Prakash et al., 2015; Ricciardulli & Garcia, 2000; Tost et al., 2006; Yokoyama et al., 2014). LHR of the reanalyses in the lower troposphere was reported to be larger than that based on Tropical Rainfall Measuring Mission (TRMM; Simpson et al., 1996) data (Jiang et al., 2011; Yokoyama et al., 2014), and this discrepancy also existed in MERRA-2 (Huaman & Schumacher, 2018). Ricciardulli and Garcia (2000) showed that the high-frequency signals of equatorial waves from the Community Climate Model are significantly weaker than the variabilities in outgoing longwave radiation. Li et al. (2009) revealed that the lack of global models for predicting the Madden-Julian oscillation (MJO) is largely attributed to the uncertainties in LHR from the convective parameterization. More recently, Cui et al. (2017) and Prakash et al. (2015) reported that large uncertainties in the precipitation in the reanalysis data stem from the uncertainties in convective parameterization.

As CGWD parameterization requires convective cloud information as input parameters, uncertainties in the cloud information of the reanalysis inevitably afford uncertainties in the CGWMF. Therefore, realistic cloud information, including LHR profile, is required for realistically representing CGWs. The LHR of a convective cloud is difficult to directly observe; thus, several studies indirectly detected it using precipitation variables. The hydrometeor heating (HH) algorithm is the first known method for obtaining vertical profiles of LHR from evaporation, melting, condensation, and deposition processes (Tao et al., 1990). Thereafter, Tao et al. (1993) proposed a convective-stratiform heating (CSH) algorithm that estimates LHR profiles from lookup tables (LUTs) in the tropical region using the surface precipitation and stratiform rain rates. The CSH algorithm has been improved by updating LUTs using additional simulations (Lang & Tao, 2018), which better corresponds to the Global Precipitation Measurement (GPM; Hou et al., 2014) mission, the follow-up of the TRMM. Afterward, LHR profiles in the midlatitudes became available via the additional construction of extratropical LUTs (Tao et al., 2019).

Recently, Alexander et al. (2021) calculated CGWMF through offline calculations using LHR profiles of TRMM and online calculations using the Whole Atmosphere Community Climate Model version 6. They compared the offline and online CGWMF with GW momentum flux observed in superpressure balloons in the tropical regions (15°N–15°S). Since GPM data cover the region from the tropics to midlatitudes, unlike the TRMM data that exclusively observed tropics and subtropics, the use of GPM data is ideal for investigating the global impacts of LHR on CGWMF. Investigating the global CGWMF is important as the magnitude of CTMF in the midlatitude storm tracks during the wintertime is comparable to or even larger than that in the tropical regions (e.g., Choi & Chun, 2013; KCK17; Song et al., 2007).

In this study, we examine the spatiotemporal variation of GPM-LHR between 65°N and 65°S, the GPM core observatory satellite coverage, and we calculate CGWMF and CGWD using the offline CGW parameterization by KCK17. The results are compared with those calculated using the LHR afforded by MERRA-2. This paper is organized as follows. In Section 2, GPM CSH and reanalysis data and the offline CGW parameterization by KCK17 are explained. In Section 3, the spatiotemporal characteristics of GPM-LHR are provided, and CGWMF and CGWD calculated using GPM are presented, which are compared with the MERRA-2 results. Section 4 provides the discussion, and Section 5 presents the summary and conclusions. The abbreviations used in this study are listed in Table A1.

2. Data and Methodology

2.1. GPM CSH

In this study, we used GPM V6 Level 3 gridded CSH (3GCSH; GPM Science Team, 2017a), which is a 0.25° gridded data with 1.5 hr intervals, covering 65°N–65°S horizontally and 80 vertical levels extending up to 20 km from the surface. The GPM 3GCSH data for 6 yr from June 2014 to May 2020 are used in the present study, which were downloaded from NASA (<https://disc.gsfc.nasa.gov>). The process to derive GPM 3GCSH can be found in the Release Notes for the CSH V6 Level 2 pixel product (2HCSH) and Level 3 gridded (3GCSH) products (<https://arthurhou.pps.eosdis.nasa.gov/GPMprelimdocs.html>). Figure S1 in Supporting Information S1 displays the satellite trajectory and the number of satellite observations per month in each grid point. The number of times that satellite passed each grid point, shown in Figure S1 in Supporting Information S1, was calculated by counting the GPM 3GCSH data in each grid cell (0.25° × 0.25°) for 6 yr. The GPM passes grid cells at the equator 6.7 times per month, denoting that the temporal resolution of the GPM data is about 4–5 days (Figure S1c in Supporting Information S1). Therefore, in this study, analysis and comparison are made using a monthly averaged unconditional mean that considers all data in all grid cells, regardless of the existence of clouds. An exception is made for the heating maximum height (Figure 3c), which is averaged only when a cloud exists. This is because when the unconditional mean is applied to the heating maximum height, the heating maximum height is artificially lowered in areas where the frequency of cloud occurrence is low.

In GPM 3GCSH, the cloud top (bottom) height is set as the altitude where the LHR falls to 10% (0 K s⁻¹) of column-maximum heating rate (CMHR), following the method of Stephan and Alexander (2015). As GPM 3GCSH data contain the heating rate from both convective and stratiform clouds, several criteria are applied to GPM 3GCSH to derive LHR of convective clouds, following Kang et al. (2020) who estimated the LHR of convective clouds using the air temperature tendency due to moist processes (DTDTMST) provided from MERRA-2 data. The profile is considered as LHR induced by deep convective clouds when (a) the height of LHR maximum is higher than 850 hPa, (b) cloud top height is higher than 700 hPa, (c) cloud-bottom height is lower than 7 km, and (d) cloud depth is deeper than 1 km.

Additionally, CGWMF and CGWD are calculated using TRMM V6 Level 3 gridded CSH (TRMM 3GCSH; TRMM, 2019), which is a TRMM product of the same format as GPM. Except that the input data is TRMM 3GCSH, it is calculated in the same process as calculation using GPM 3GCSH, and the comparison between GPM and TRMM will be discussed in Section 4.3.

2.2. Reanalysis Data

MERRA-2 pressure level (42 levels from 1,000 to 0.1 hPa) data with a longitudinal (latitudinal) resolution of 0.625° (0.5°) provided by 3 hr intervals are used in the present study over the same 6 yr period (June 2014 to May 2020). The variables used from MERRA-2 are the zonal and meridional wind, geopotential height, air temperature, cloud top height, and DTDTMST, which represents a diabatic forcing (Bosilovich et al., 2016). To obtain LHR by convective clouds from DTDTMST, the aforementioned criteria applied to GPM 3GCSH are employed. The cloud top and bottom heights are determined from the DTDTMST profile rather than simply using the MERRA-provided cloud top height due to some uncertainties, as discussed in Kang et al. (2020). The cloud top (bottom) is defined as an altitude where DTDTMST falls to 20% (5%) of CMHR, but it is constrained to not be higher than the cloud top height provided from MERRA-2.

The MERRA-2 wind and temperature variables are used for the background fields to calculate the offline CGWD parameterization using both the LHR information from GPM 3GCSH and DTDTMST of MERRA-2. To investigate the sensitivity of the background fields, ECMWF Reanalysis v5 (ERA5) pressure level data from 1,000 to 1 hPa with 37 vertical levels and horizontal resolution of 0.25° (Hersbach et al., 2020) are additionally used.

2.3. Offline CGW Parameterization

The CTMF is calculated using the formulation by KCK17:

$$M_{ct}(c, \varphi) = \operatorname{sgn}[c - U_{ct}(\varphi)] \rho_{ct} \frac{2(2\pi)^3}{A_h L_t} \left(\frac{g}{c_p T_q N_q^2} \right)^2 \frac{N_{ct} |X|^2}{|c - U_{ct}(\varphi)|} \Theta(c, \varphi) F(\mu). \quad (1)$$

Here, c is the ground-based phase speed in the azimuthal direction of wave propagation, $\varphi \cdot U_{ct}(\varphi)$ is the basic-state wind projected in the φ direction at the cloud top, L_t is the time scale, A_h is the horizontal area, ρ_{ct} is the air density at the cloud top, c_p is the specific heat capacity of air at constant pressure, g is the gravitational acceleration, and T_q is the temperature averaged over the diabatic forcing region. N_q and N_{ct} are the Brunt-Väisälä frequency in the diabatic forcing region and at the cloud top, respectively. All the constants are the same as in the previous studies (CC11; KCK17). An important factor in CTMF is $N_{ct}|X|^2/|c - U_{ct}(\varphi)|$, the wave-filtering and resonance factor (WFRF; Song & Chun, 2005). It represents both critical-level filtering effects in the diabatic forcing region and the resonance between the natural modes given by the dispersion relation of the internal GWs and vertical harmonics that are determined via convective forcing (see details in Song & Chun, 2005). The second important factor is $\Theta(c, \varphi)$, the convective source spectrum, which is expressed as:

$$\Theta(c, \varphi) = q_0^2 \left(\frac{\delta_h \delta_t}{32\pi^{3/2}} \right)^2 \frac{1}{1 + [c - c_{qh}(\varphi)]^2 / c_0^2}. \quad (2)$$

$\Theta(c, \varphi)$ is derived from a specified diabatic forcing with a Gaussian-shaped function in time and space (Song & Chun, 2005). In Equation 2, q_0 is the amplitude of heating, and $c_{qh}(\varphi)$ is the moving speed of convective heating. c_0 represents the width of the convective forcing spectrum, defined as δ_h / δ_t , where δ_t and δ_h correspond to the time and spatial scales of the forcing, respectively. Here, q_0 is determined as follows:

$$q_0 = H_{\max} c_f c_p, \quad (3)$$

where H_{\max} is the CMHR. The conversion factor, c_f , is needed for matching the calculated CTMF based on Equation 1 to the observed GW momentum flux. In Kang et al. (2020), c_f was set to 350 based on the superpressure balloon observation data near 50 hPa and 10°N–10°S from 8 February to 11 May 2010 reported by Jewtoukoff et al. (2013).

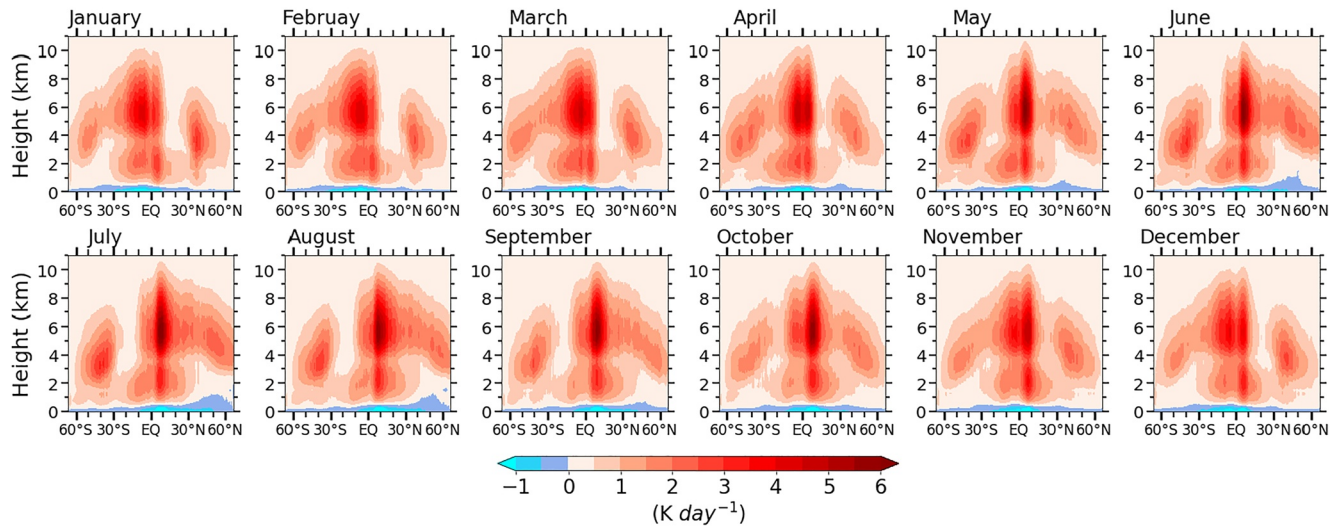
As recent study by Corcos et al. (2021) noted that the superpressure balloon data of Jewtoukoff et al. (2013) are biased, c_f in the present study is set based on the superpressure balloon observation data by Corcos et al. (2021) during 6 December 2019 to 28 February 2020 in which the period is overlapped with the current study. We set $c_f = 350$ in the calculation of CTMF using the MERRA-2 cloud information, which is the same as that used in Kang et al. (2020), while c_f is set to 268 in the calculation of CTMF using the GPM cloud information to make sure that the averaged CGWMF using the GPM cloud information is the same as that using the MERRA-2 cloud information between 10°N and 10°S at 50 hPa from 6 December 2019 to 28 February 2020. Although different c_f is specified for GPM and MERRA-2, the averaged CGWMF of both GPM and MERRA-2 are about 2.5 mPa over the same location from June 2014 to May 2020, which is similar to that averaged from 6 December 2019 to 28 February 2020. Note that increases in c_f will increase the magnitude of the CTMF, and this is generally true for the CGWMF and CGWD, although its impact is not linearly correlated with CGWMF and CGWD. That is, the result is sensitive to the choice of c_f , and more observational data sets of GWMF such as superpressure balloons for longer period are required for deriving robust value of c_f . Finally, $F(\mu)$ in Equation 1 represents the nonlinear effect of CGWs. The details can be found in KCK17.

3. Results

3.1. Latent Heating Rates From GPM 3GCSH

Figure 1 shows the zonal-mean LHR, which contains all clouds, for each month averaged for 6 yr (June 2014 to May 2020) and their standard deviations. The maximum LHR for each month is generally at 0°–10°N with the largest LHR being 6.3 K day⁻¹ in July at $z = 6$ km. The vertical extent of the large LHR (>0.5 K day⁻¹) is the greatest in the tropical regions, especially in the intertropical convergence zone (ITCZ) with a heating top of about 10 km. The secondary maximum of LHR is located in the winter hemisphere midlatitudes, with a top of 6–7 km. In these regions, the largest LHR is 3.1 K day⁻¹ in June, which is located at $z = 4$ km at 39°S, corresponding to the Southern Hemisphere (SH) winter storm tracks. In the summer midlatitudes, convective activity is strong over land, with a maximum of 2.4 K day⁻¹ at $z = 5.5$ km in June. The standard deviations (Figure 1b) are considerable near the equator where LHR is significantly large, with the maximum value of 1.2 K day⁻¹ at 10°N in May. The large standard deviations in the equatorial regions are likely attributed to the strong interannual variabilities of the convective activities associated with QBO and El Niño-Southern Oscillation (Lee et al., 2019; Liess & Geller, 2012).

(a) Monthly-mean LHR



(b) Standard deviations

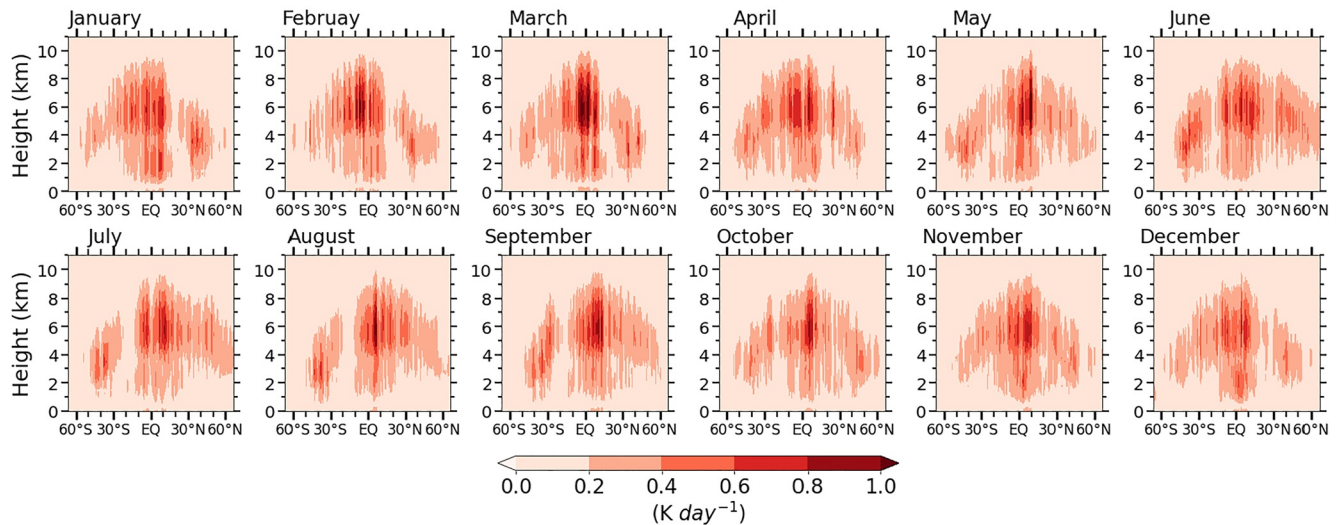


Figure 1. Latitude-height cross sections of (a) the zonal-mean latent heating rate (LHR) averaged for each month during June 2014 to May 2020 and (b) their standard deviations.

Figure 2 presents the probability density functions of the cloud (a) top and (b) bottom heights and (c) depth from all clouds based on the GPM 3GCSH (hereafter GPM) data between 65°N and 65°S for 6 yr (June 2014 to May 2020). Black, red, and blue colors denote all seasons, June–July–August (JJA), and December–January–February (DJF), respectively. The cloud top height of 4 km is most frequently observed, while that of 9 km is the second-most frequently observed (Figure 2a). A cloud-bottom height of less than 1 km is dominant: 65% for all cases and 59% for JJA (Figure 2b). The heating depth of 3–4 km is the most frequent, followed by a depth of 5–7 km (Figure 2c). Although seasonal differences are not clear, some differences exist between JJA and DJF. First, the occurrence of cloud top height above (below) 9 km increases (decreases) in JJA, while it decreases (increases) in DJF. Second, in JJA (DJF), cloud-bottom heights higher (lower) than 2 km are more abundant than that in any other season. Third, cloud depths of 7–9 km occur more frequently (rarely) in DJF (JJA) than that in other seasons. This is because the cloud-bottom in JJA is lifted up from the surface despite the frequent occurrence of high cloud top heights.

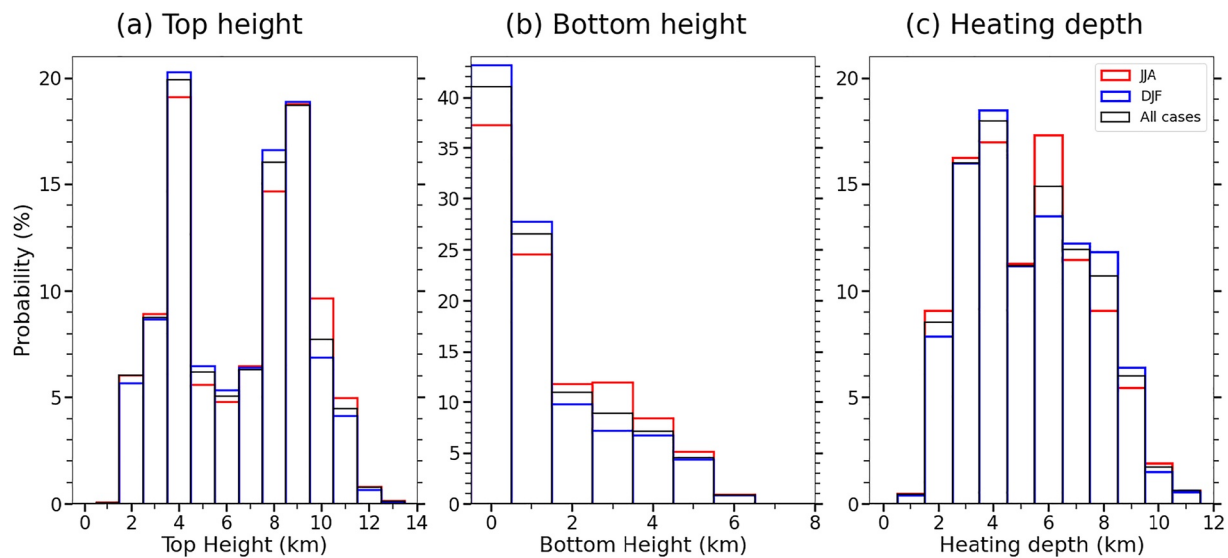


Figure 2. Histograms of (a) the heating top height, (b) the heating bottom height, and (c) the heating depth between 65°N and 65°S. The bin interval is 1 km, and black rectangles indicate all GPM 3GCSH observation cases. The blue (red) rectangles indicate DJF (JJA).

Figure 3 displays the CMHR, which contains all clouds, in the GPM data (Figure 3a) and the height where the CMHR occurs (Figure 3c), averaged from June 2014 to May 2020. Figures 3b and 3d are the standard deviations of Figures 3a and 3c, respectively. Large values of CMHR are distributed along the equatorial region, with the maximum zonal-mean value of 7.3 K day⁻¹ at 6°N. The secondary peak of the zonal-mean CMHR is located at 3°S. The primary and secondary peaks of the zonal-mean CMHR averaged over the 6 yr are related to the ITCZ (Figure 3a). The standard deviations of CMHR (Figure 3b) are generally large where the CMHR is large, indicating the intermittent nature of convective activities. However, several regions with relatively large standard deviations exist but with a relatively small magnitude of CMHR, especially over land: East-north America, South

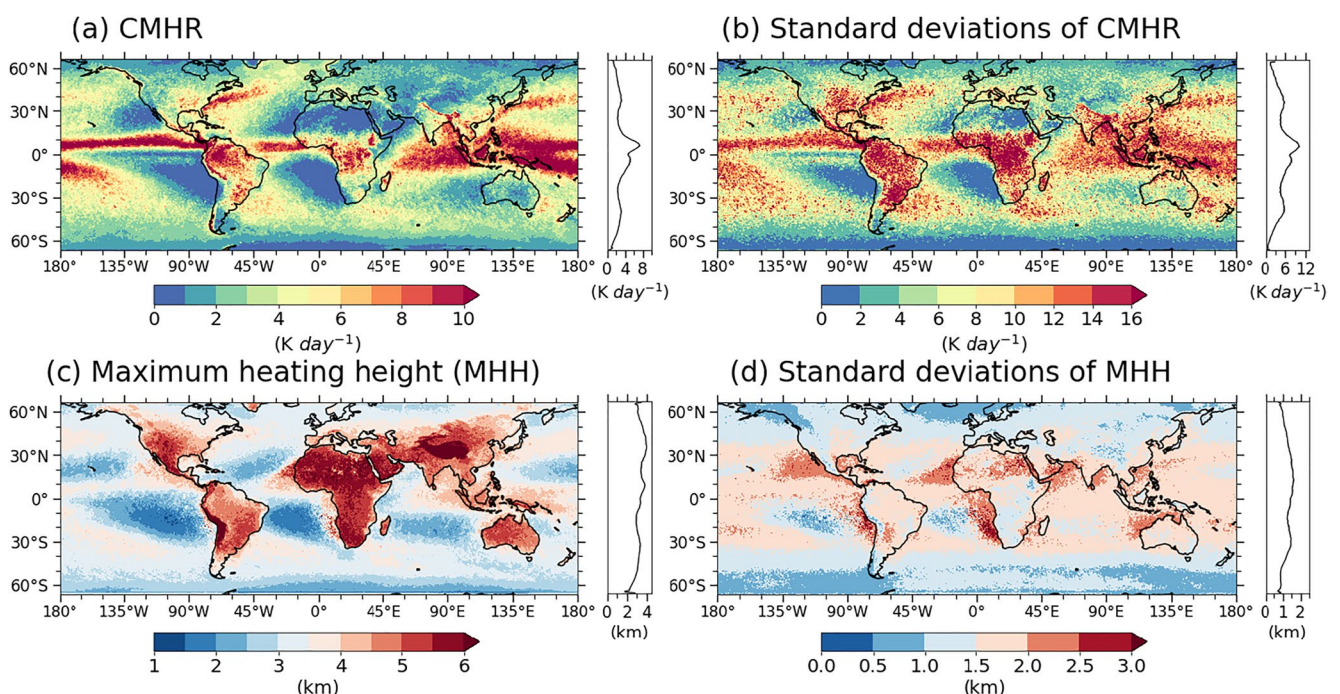


Figure 3. Global distributions of (a) column-maximum heating rate (CMHR) and (c) heating maximum height calculated using GPM 3GCSH averaged from June 2014 to May 2020. (b and d) exhibit standard deviations of (a and c), respectively. The zonally averaged values are plotted to the right of each plot.

America, South Africa, India, and South China. The zonally averaged heating maximum height (Figure 3c) is about 4 km at 35°N mainly due to the Rocky Mountains and the Himalayas, while the minimum height is 1.8 km at 65°S, where the Antarctic circumpolar current flows are present. The maximum heating height is generally higher over the land than the ocean, which is similar to the result of Liu et al. (2022) using TRMM spectral latent heating. The standard deviation of the maximum heating height (Figure 3d) is large in regions with small CMHR (e.g., eastern Pacific and Atlantic regions, western coast of Indian Ocean, and Sahara Desert), primarily due to the rare occurrence of deep convections.

Figure 4 displays the time series of the zonally averaged monthly mean CMHR in each latitudinal bin and their power spectral densities (PSD) from GPM and MERRA-2 DTDTMST (hereafter MERRA-2). CMHR value averaged over the entire period is given in the top right of each panel (blue) in Figures 4a and 4c, and the correlation coefficient between the CMHR time series of GPM and MERRA-2 is given in the top right of Figure 4c (black). We only consider CMHR profiles that the heating maximum height is higher than 850 hPa to eliminate the effects of strong LHR of MERRA-2 in the lower troposphere (Huaman & Schumacher, 2018). Figures 4a and 4b exhibit some interesting features. First, even in the same equatorial region, the characteristics of CMHR in 0°–10°N

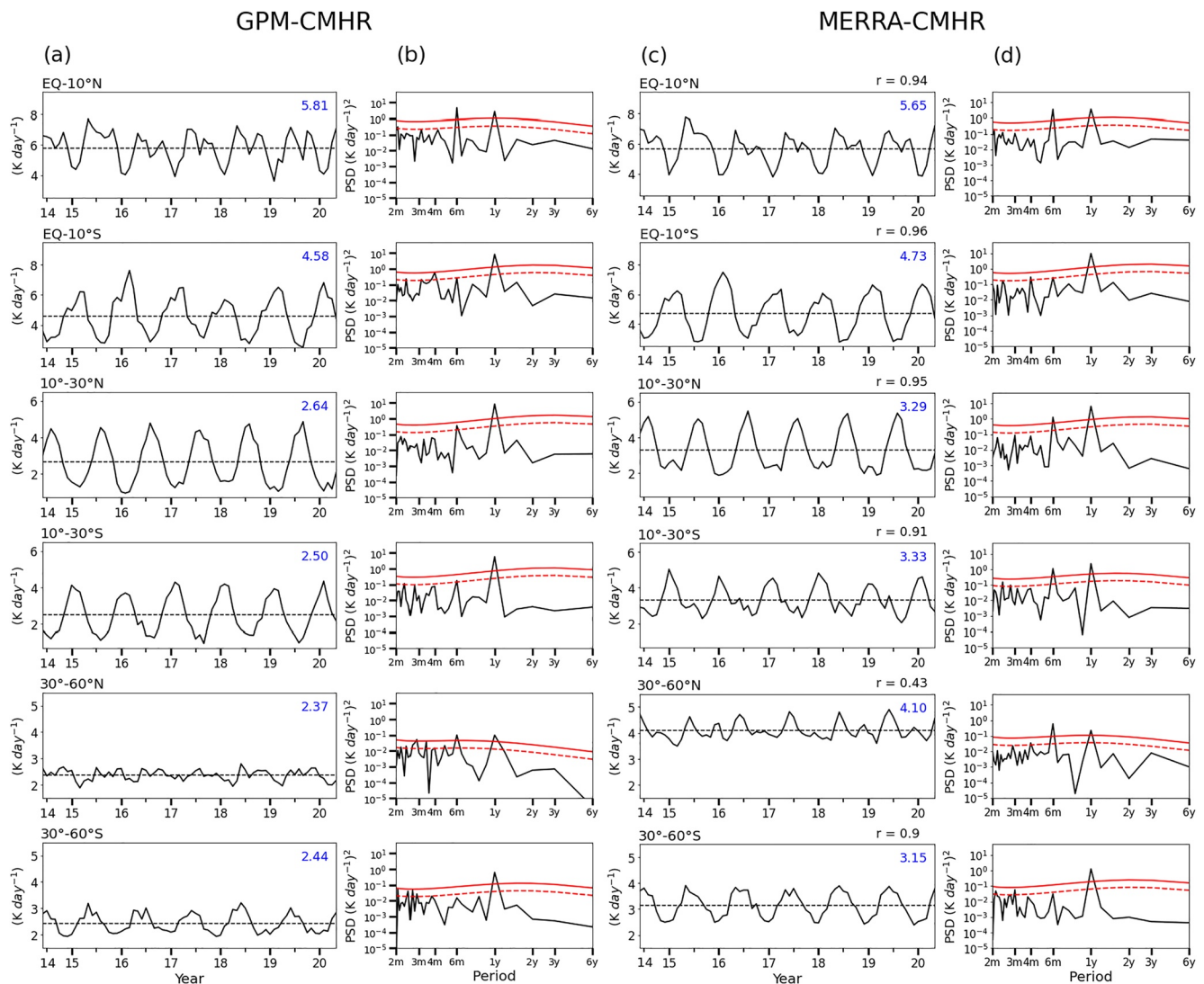


Figure 4. (a) Time series of column-maximum heating rate (CMHR) based on Global Precipitation Measurement (GPM) from June 2014 to May 2020, and (b) the power spectral densities (PSD) of each CMHR averaged over 0°–10°N, 0°–10°S, 10°–30°N, 10°–30°S, 30°–60°N, and 30°–60°S. Black dashed line in (a) denotes the mean values of each metric. Red dashed (solid) line in (b) denotes the red noise spectra (red noise spectra at the 95% confidence level). (c and d) are similar to (a and b) but for Modern-Era Retrospective Analysis for Research and Applications, Version 2 (MERRA-2).

and 0°–10°S are different. The mean value of CMHR is larger in 0°–10°N than that in 0°–10°S (Figure 4a), and the semi-annual (annual) cycle is dominant in 0°–10°N (0°–10°S; Figure 4b). This result is consistent with that of Mitchell and Wallace (1992), who stated that the semi-annual cycle of the equatorial convection, represented by outgoing longwave radiation, was clear in the Northern Hemisphere (NH) but not in the SH. Second, no apparent periodicity is associated with QBO near the equator, which can be explained by two possibilities. (a) Since the response of the convective activities to the QBO phase varies with longitudes (Lee et al., 2019; Liess & Geller, 2012), the zonally averaged CMHR may not exhibit statistically significant spectral peaks at periods related to QBO. Additionally, (b) the data period (June 2014–May 2020) includes the 2015/2016 (Kang et al., 2020; Newman et al., 2016; Osprey et al., 2016) and 2019/2020 (Kang & Chun, 2021) QBO disruption events that temporarily changed the QBO cycle, which possibly made the spectral peak at ~28 months unclear. Third, in the subtropical regions, CMHR is strong in the summer and weak in the winter in both hemispheres, and therefore, the annual cycle is dominant. Fourth, in the midlatitudes, CMHR exhibits weak seasonal variation in both hemispheres; however, the variation in SH is more pronounced than that in NH. CMHR in the NH midlatitude is dominated by a semi-annual cycle, which is due to a half-year phase difference in the convective activity between land and ocean (Jalihal et al., 2019). In the SH midlatitude, the land heating effect is smaller than that in the NH, affording a dominant annual cycle related to ocean heating.

The CMHR of GPM is generally similar to that of MERRA-2. First, the equatorial regions exhibited strong CMHR during 2015–2016. Second, in the subtropical regions, the annual cycle is dominant, and third, seasonal variation is relatively small in the midlatitudes. However, the CMHR of MERRA-2 is larger than that of GPM, except for the tropical regions. Correlation coefficients between GPM and MERRA-2 are greater than 0.90 for all latitude bins, except for 30°–60°N where it is 0.43 (Figure 4c). The largest difference is in the NH midlatitude (30°–60°N) during summer (June–July), mainly over the land: the CMHR of MERRA-2 is greater by 7 K day⁻¹ than that of GPM at 90°–110°E during summer (Figure S2 in Supporting Information S1), which is likely because of uncertainties in the convective parameterization employed in GCM (Cui et al., 2017; Prakash et al., 2015; Tost et al., 2006).

3.2. Cloud Top Momentum Flux

Figure 5 shows the absolute CTMF calculated using GPM (hereafter GPM-CTMF) and MERRA-2 (hereafter MERRA-CTMF) in January and July, and the differences between the two. The panel on the right side of each plot represents the zonally averaged values. The maximum value of the zonally averaged GPM-CTMF is 16.0 (14.1) mPa at 36°N (38°S) in January (July) in the storm track regions, with the secondary maximum of 5.9 (9.8) mPa at 5°S (9°N) near the equator. Notably, the CMHR is maximum near the equator, whereas the CTMF is maximum in the winter hemisphere midlatitudes, as in several previous studies (e.g., Choi & Chun, 2013; KCK17). This stems from three major factors. First, the CTMF is determined by the spectral combination of WFRF and the convective source, which is maximal in the midlatitudes as WFRF is considerably larger in the midlatitudes than that in the equatorial regions. Second, the nonlinear forcing effect is strong near the equator where convection is strong, and therefore, the magnitude of CTMF reduces by a small $F(\mu)$ term in the equatorial regions. Third, the term $(g/c_p T_q N_q^2)^2$ in Equation 1 is larger in the winter midlatitudes than the equatorial regions: 0.13 (0.13) kg² J⁻² m² in the midlatitudes and 0.07 (0.08) kg² J⁻² m² in the equatorial regions in January (July), respectively. This result is consistent with that of Kang et al. (2017). In July, the GPM-CTMF averaged over 30°–60° is 6.6 mPa in the SH, which is significantly larger than the 5.5 mPa in the NH. This is similar to several previous studies on the GW momentum flux estimated from satellite data, which exhibits a predominant magnitude in the SH winter midlatitudes, including areas of GW hotspots (e.g., Ern et al., 2011; Hindley et al., 2015; Hoffmann et al., 2013).

Several differences exist between GPM-CTMF and MERRA-CTMF in each latitude bin. In the equatorial regions (10°N–10°S), GPM-CTMF is 4.7 (4.5) mPa in January (July), which is smaller than 6.0 (6.2) mPa of MERRA-CTMF. In the winter hemisphere midlatitudes (30°–60°), GPM-CTMF is 6.5 (6.6) mPa in January (July), which is much larger than 4.8 (3.6) mPa of MERRA-CTMF. Consequently, near the equator, MERRA-CTMFs are overestimated compared to GPM-CTMFs, while they are underestimated in the winter hemisphere midlatitudes.

In Figure S3 in Supporting Information S1, the eastward, westward, northward, and southward CTMF in January and July are shown. In the equatorial (storm track) regions, the largest contribution to the total momentum flux is from the eastward (westward) momentum flux in both January and July. Considering MERRA-CTMF,

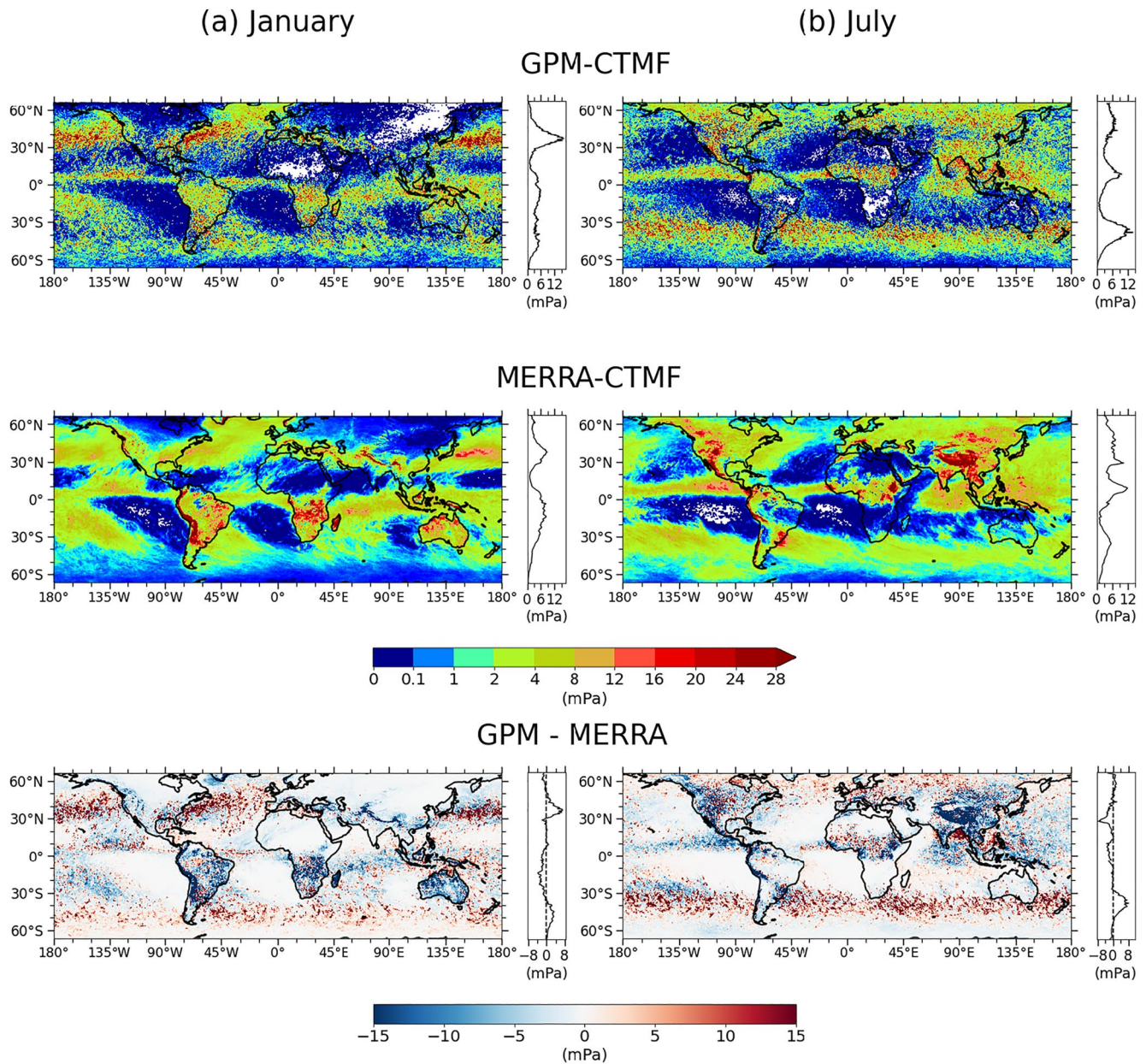


Figure 5. Global distributions of the 6 yr (June 2014 to May 2020) averaged absolute cloud-top momentum flux (CTMF) calculated using the Global Precipitation Measurement (GPM; top) and Modern-Era Retrospective Analysis for Research and Applications, Version 2 (MERRA-2; middle) latent heating rate (LHR) data, and their differences (bottom) in (a) January and (b) July. The zonally averaged values are plotted to the right of each plot.

the westward momentum flux is considerably smaller than GPM-CTMF in the storm track, while the eastward momentum flux is slightly larger than GPM-CTMF in the equatorial region. This implies that the differences in absolute CTMF in the storm track regions between GPM and MERRA-2 are mainly due to differences in the westward momentum flux.

To examine the sensitivity of the background variables to the CTMF calculation, CTMF calculation using the horizontal wind, geopotential height, air temperature from ERA5 is performed using the GPM convective heating information. The GPM-CTMF using ERA5 background variables is similar to (not shown) that obtained using MERRA-2 background variables. The correlation coefficient between the zonal-mean GPM-CTMF using ERA5 and the original GPM-CTMF is 0.989 and 0.994 in January and July, respectively, denoting that the effect of the background field differences due to the different reanalysis data on CTMF is negligible.

Figure 6 is similar to Figure 4 except for the absolute CTMF. Characteristics of GPM-CTMF are different from those of CMHR in terms of magnitude and temporal variability. First, while the 6 yr averaged CMHR is maximal near the equator (Figure 4a), the CTMF magnitude is maximal in the NH midlatitude (Figure 6a). Second, in the NH midlatitude (30°–60°N), CMHR is slightly larger during JJA than that during DJF, while the opposite is true for CTMF. This is because CTMF is maximized in the storm track regions in the winter (Figure 5a). Furthermore, only the semi-annual cycle is statistically significant in CTMF (Figure 6b), which differs from the statistically significant semi-annual and annual cycles in CMHR.

The differences between GPM-CTMF and MERRA-CTMF for each latitude bin are analyzed. GPM-CTMF is generally smaller than MERRA-CTMF, except for the midlatitudes (Figures 6a and 6c). The most significant difference in the absolute CTMF is in the SH midlatitudes: GPM-CTMF (4.9 mPa) is 1.7 times larger than MERRA-CTMF (2.9 mPa), despite the CMHR of GPM being about 30% smaller than that of MERRA-2. In the NH midlatitudes, the GPM-CTMF and MERRA-CTMF values averaged for the entire period are the same (5.6 mPa), but the temporal variability is different: MERRA-CTMF clearly exhibits an annual cycle while GPM-CTMF does not. This is due to a larger MERRA-CTMF in JJA than that in DJF, which is not evident in GPM-CTMF because GPM-CTMF is smaller and larger than MERRA-CTMF in JJA and DJF, respectively. Correlation coefficients between GPM-CTMF and MERRA-CTMF in each latitude bin are smaller than those between the CMHR of GPM and MERRA. This is somehow expected, as the spectral combination of CMHR and WRF determines CTMF, and the cloud top and bottom heights, which are important factors in WRF, exhibit discrepancies between GPM and MERRA-2. The lowest correlation coefficient can be found in the NH midlatitude with a value of 0.04.

Figure 7 shows the zonal-mean convective source, WRF, and CTMF spectrum in (a) January and (b) July for GPM-CTMF (upper) and MERRA-CTMF (lower). The zonal-mean convective source spectrum of GPM is considerably stronger than that of MERRA-2 in most latitudes, due to the more frequent occurrence of extremely large CMHR in GPM (Figure S4 in Supporting Information S1). On the other hand, the WRF of MERRA-2 is generally larger than GPM, except in the SH mid-to-high latitudes. As CTMF is determined by the spectral combination of convective source and WRF, the differences in the CTMF spectrum between GPM and MERRA-2 are not as dominant as those in the convective source spectrum.

The WRF of GPM is somewhat different from that of MERRA-2. Note that WRF is calculated using the background variables as well as cloud top and bottom heights, and the differences in WRF between GPM and MERRA-2 stem from cloud top and bottom heights information, as the same background variables are used for both calculations. The 6 yr averaged cloud depth at 10°N–10°S using GPM is slightly deeper than that using MERRA-2, but their differences increase with the latitude (Figure S5 in Supporting Information S1). As relatively deep convective forcing makes WRF large at high phase speeds and small at low phase speeds (Kang et al., 2017; Song & Chun, 2005), deeper convective clouds of GPM can be expected to afford relatively strong power at high phase speeds. Indeed, the relatively strong power of WRF at high phase speeds is evident in GPM poleward of 30°S in the SH, especially for the eastward propagating component, and near 30°N in January for phase speeds larger than 40 m s⁻¹. Moreover, the relatively weak power of WRF with low phase speeds (smaller than ~20 m s⁻¹) is evident in GPM poleward of 30°N during both January and July, compared to that in MERRA-2.

In January (July), WRF is larger in MERRA-2 than in GPM at latitudes northward of 30°N (5°S), due to the more frequent occurrence of deep convections in MERRA-2. In January (July), the probability of deep convection occurring in each grid averaged between 30° and 60°N (5°S–60°N) is 11% (14%) for GPM and 18% (23%) for MERRA-2. Furthermore, in the SH midlatitudes (30°–60°S) in July, the probability of deep convection is 15% for GPM and 10% for MERRA-2, indicating that deep convection events in the SH midlatitudes may be underestimated in MERRA-2 (not shown). The CTMF spectrum clearly displays stronger magnitudes in the winter hemisphere midlatitudes, especially near 40°, and stronger powers at high phase speeds at most latitudes for GPM than for MERRA-2.

3.3. CGW Momentum Flux and Drag Above Cloud Top

The CGWMF above the cloud top is calculated using Lindzen's linear saturation theory (Kang et al., 2017; Lindzen, 1981). Figure 8 displays the 6 yr mean of the eastward and westward CGWMF at the cloud top and four

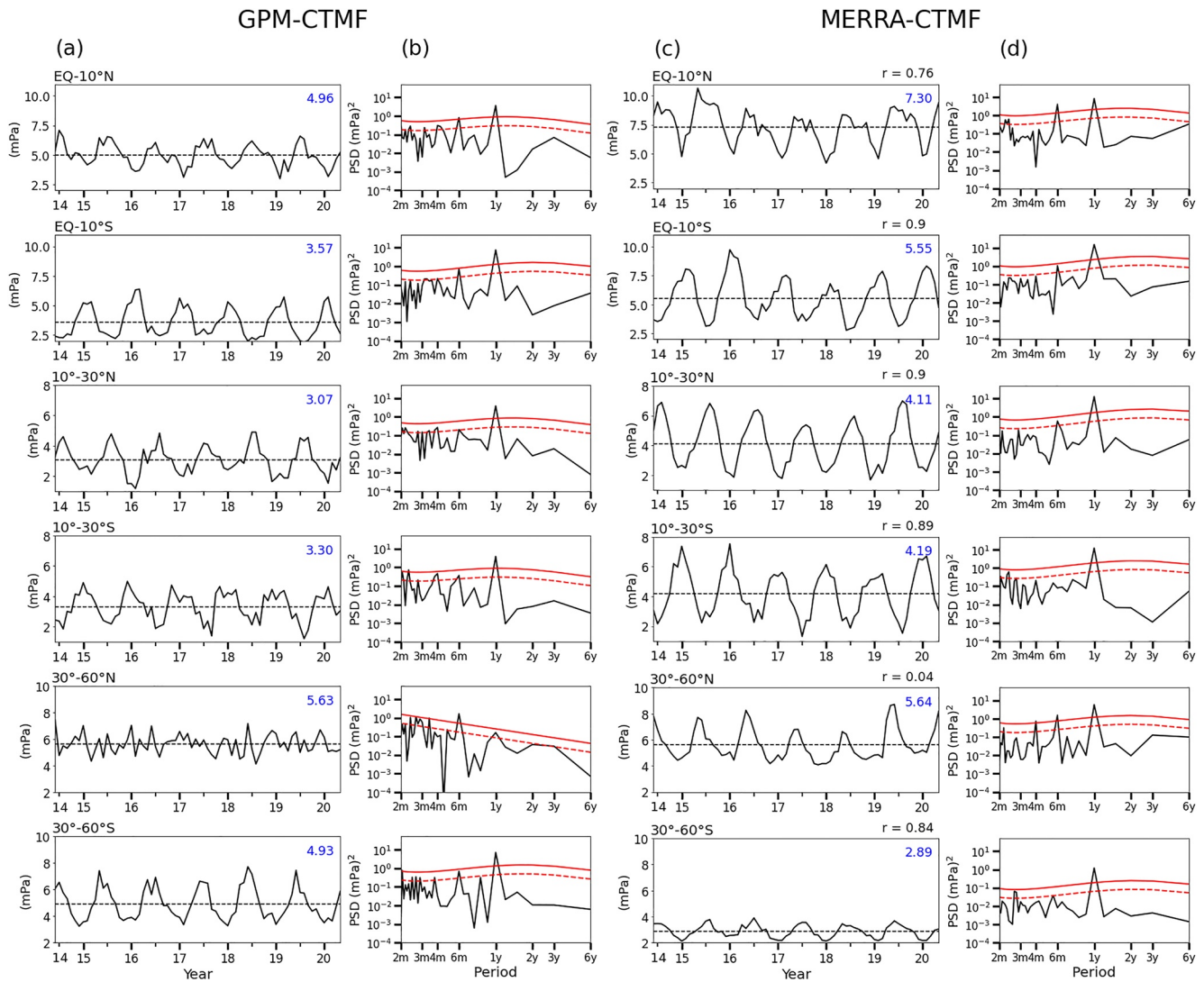


Figure 6. Same as in Figure 4 but for absolute cloud-top momentum flux (CTMF).

selected levels above the cloud top (50, 10, 1, and 0.3 hPa) in (a) January and (b) July. In January (Figure 8a), the eastward momentum flux above the cloud top is maximal at 9°S, although that at the cloud top is maximal in the midlatitude. This is due to that the eastward momentum flux in the storm track region is almost filtered between the cloud top (~400 hPa) and each height above the cloud top due to westerly winds in the NH winter. In contrast, in the equatorial region, CGWMF is less filtered from the cloud top to each height above the cloud top due to the presence of weak easterly winds. This situation is different for the westward momentum flux. A single peak locates at the NH storm tracks for CTMF, and the peak remains during the propagation above the cloud top under the westerly background wind in the NH winter middle latitude, although its magnitude reduces with height due to the wave dissipation processes.

Comparison between GPM and MERRA-2 reveals that both the eastward and westward GPM-CTMF are generally smaller than MERRA-CTMF in most regions, except in the midlatitudes. The most significant difference between the two is in the NH storm track region near 36°N where the zonally averaged westward (eastward) momentum flux of GPM-CTMF is 6.0 (2.0) mPa compared with 3.1 (1.3) mPa of MERRA-CTMF. Additionally, the westward momentum flux of GPM in the storm tracks in the stratosphere is larger than that of MERRA-2, as its magnitude at the cloud top is larger.

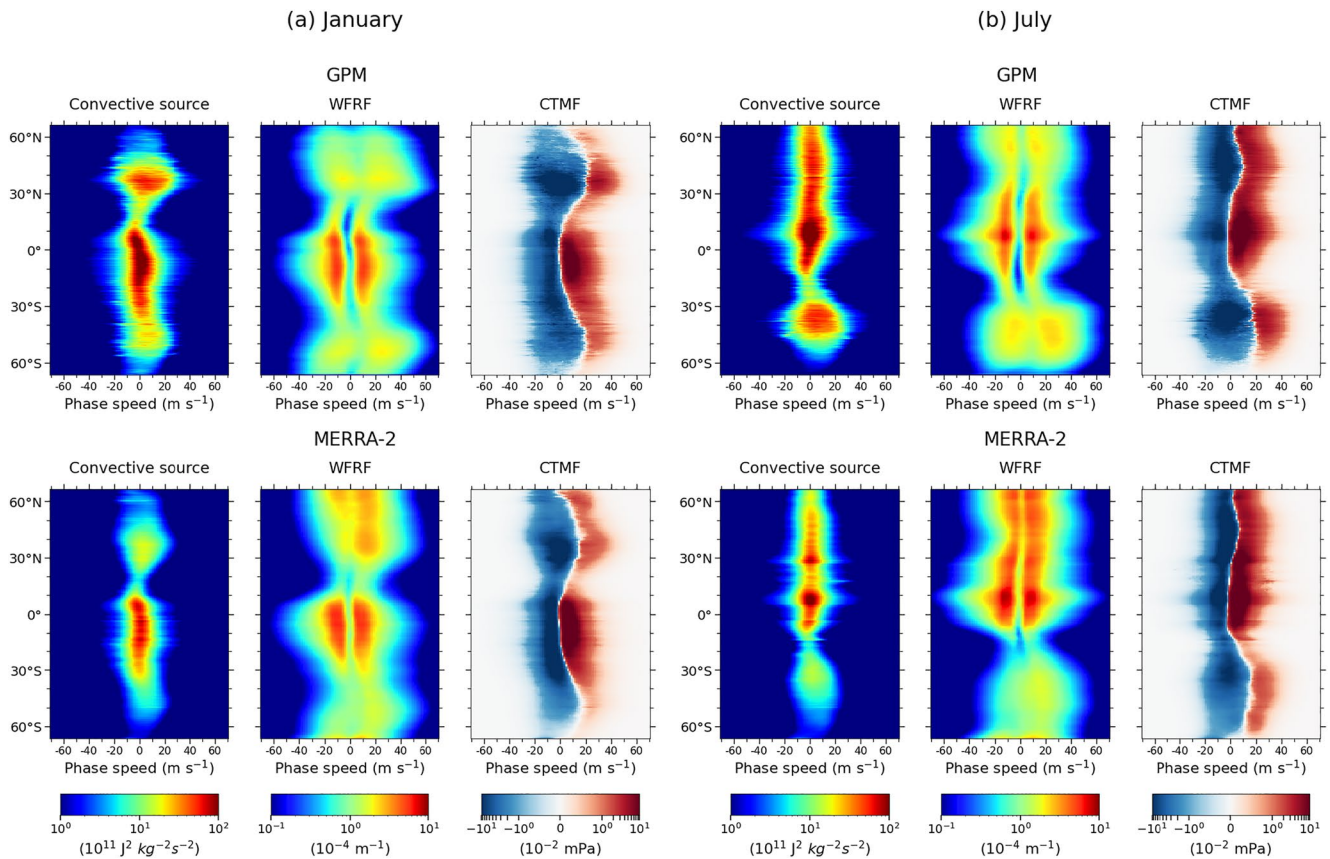


Figure 7. Latitudinal distributions of the zonal-mean zonal convective source, wave-filtering and resonance factor (WFRF), and cloud-top momentum flux (CTMF) spectrum calculated using Global Precipitation Measurement (GPM; top) and Modern-Era Retrospective Analysis for Research and Applications, Version 2 (MERRA-2; bottom) in (a) January and (b) July.

In July (Figure 8b), the result is generally similar to January, considering the seasonal changes in NH and SH. The maximum value of the zonally averaged westward (eastward) momentum flux of GPM above the cloud top in the SH midlatitudes (30°–60°S) is greater than that in the NH midlatitudes (30°–60°N) in January (Figure 8a). Using satellite data, several observational studies of the momentum flux have reported strong GW activities in the SH midlatitudes in July (e.g., Eckermann et al., 2019; Ern et al., 2011; Hocke et al., 2016; Hoffmann et al., 2016), suggesting that convection contributes to the large momentum flux there. The momentum flux of GPM in the SH storm tracks is much larger than that of MERRA-2, and its difference is larger than in the NH in January.

Recently, Corcos et al. (2021) calculated the GW momentum flux based on eight StratoLe-2 superpressure balloons observed at about $z = 20$ km near the equator from November 2019 to February 2020. 07_STR2, one of the eight superpressure balloons, flew at a mean altitude of 54.8 hPa from 6 December 2019–28 February 2020, and the averaged momentum flux for the frequency range of 15 min–1 day was 4.4 mPa. Since GWs are generated by various sources, parameterized CGWMF must be smaller than the observed GW momentum flux. The absolute momentum flux of the current GPM calculation averaged between 10°N and 10°S at 50 hPa is 2.5 mPa for the same period. This implies that the magnitude of the parameterized CGWs calculated using GPM is reasonable, which has the same order of magnitude as the observed GWs.

Figure 9 shows the zonal CGWMF spectrum at three selected levels (cloud top, 50 hPa, and 1 hPa) using GPM (red) and MERRA-2 (black) averaged over each latitudinal bin. The green line on the right of each plot represents the zonal-mean zonal wind, and the gray-shaded area represents the range of one standard deviation. Figure 10 shows the CGWD averaged over the period and location shown in Figure 9. In the equatorial region (10°N–10°S), momentum fluxes at the positive phase speeds are larger than those at the negative phase speeds for both GPM and MERRA-2 in January and July. Clearly, GPM-CTMF (MERRA-CTMF) is larger at high (low) phase speeds in the equatorial region, although the absolute GPM-CTMF is smaller than MERRA-CTMF near the equator

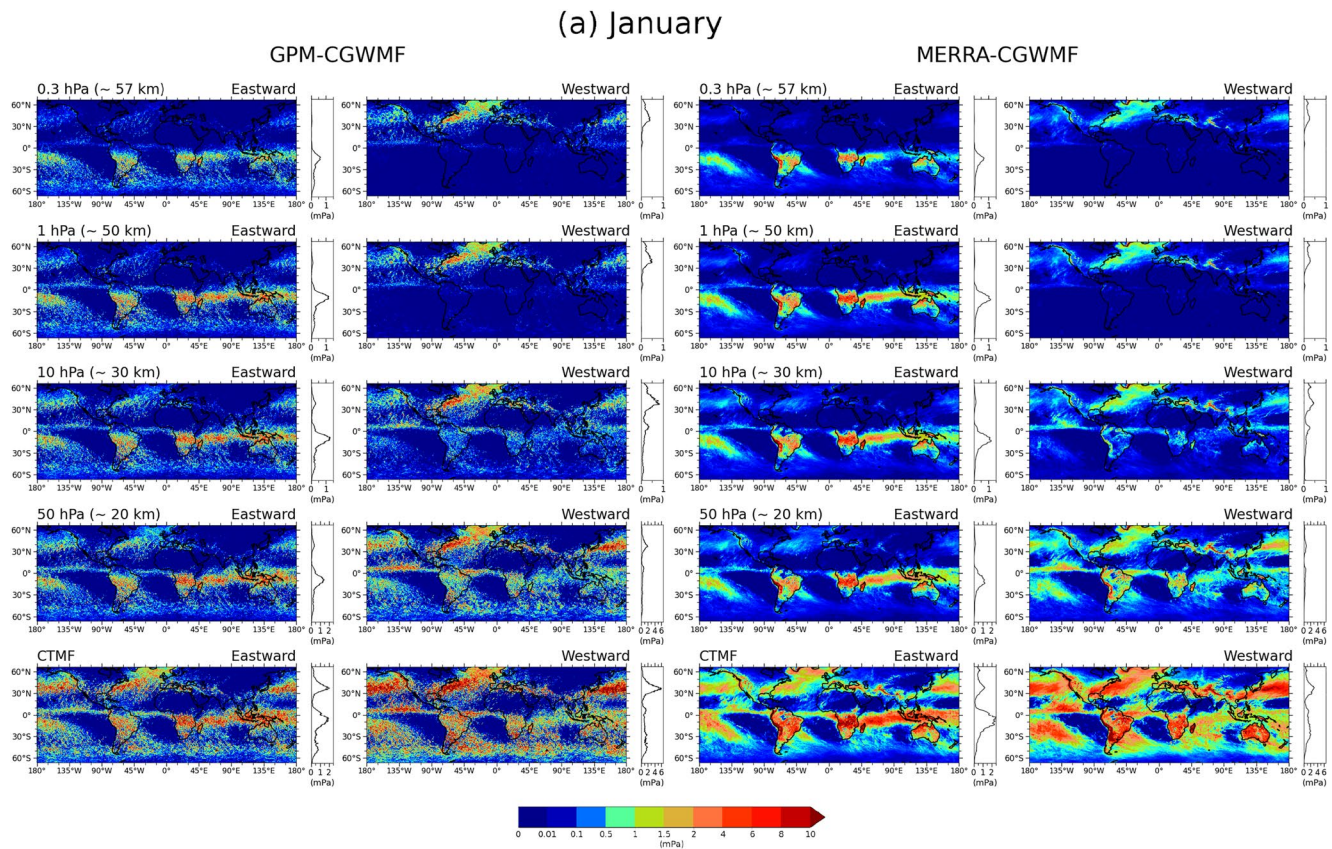


Figure 8. Global distributions of the 6 yr (June 2014 to May 2020) averaged eastward and westward convective gravity wave momentum flux (CGWMF) calculated using Global Precipitation Measurement (GPM) and MERRA-2 LHR data at the cloud top, 50, 10, 1, and 0.3 hPa (bottom to top) in (a) January and (b) July. The zonally averaged values are plotted to the right of each plot.

(Figure 6). As mentioned earlier, the larger values of GPM-CTMF at high phase speed components are due to the deeper clouds that yield WRF and resultant CTMF with stronger power at high phase speeds. The momentum fluxes at low phase speeds are mostly filtered out in the stratosphere due to weak zonal winds there, and differences in the momentum flux between GPM and MERRA-2 notably decrease with height. Since CGWD is afforded when the momentum flux is decreased, the CGWD of MERRA-2 is larger than that of GPM in the upper troposphere and lower stratosphere, approximately below 10 km (Figure 10). Momentum fluxes with negative phase speeds are almost filtered out because of the negative wind shear between 50 and 1 hPa, and only the eastward momentum flux remains at 1 hPa, providing positive CGWD to the upper stratosphere through the saturation process. As GPM-CTMF with high phase speeds is larger than MERRA-CTMF, the CGWD of GPM at $z \approx 55$ km is 3.0 (1.4) $\text{m s}^{-1} \text{ day}^{-1}$ in January (July), which is larger than 2.8 (1.3) $\text{m s}^{-1} \text{ day}^{-1}$ of MERRA-2. Recently, Ern et al. (2021) indicated that high phase-speed GWs are required in the tropics to drive the SAO in the mesosphere and mesopause region. This implies that, even if source-dependent CGWD parameterization is used, the contribution of CGWs to drive the SAO may be underestimated if unrealistic cloud information is used.

In the summer subtropics (10° – 30°), the momentum fluxes of the positive and negative phase speeds at the cloud top are almost symmetric, which is similar to the source-level spectrum assumed in the parameterization of Alexander and Dunkerton (1999). In the NH summer subtropics (10° – 30° N July), the CGWD of GPM is slightly small at 70–30 hPa. However, in the SH summer subtropics (10° – 30° S January), the two results are almost identical at altitudes above 300 hPa. In the winter subtropics (10° – 30° N January and 10° – 30° S July), the CGWD of GPM is larger than that of MERRA-2 in the stratosphere.

In the midlatitudes (30° – 60°), the positive wind shear is evident in the troposphere regardless of season; thus, the momentum fluxes with negative phase speeds at the cloud top are larger than those with positive phase speeds. In the summer (winter) midlatitude, the westward (eastward) momentum flux is dissipated by critical-level filtering

(b) July

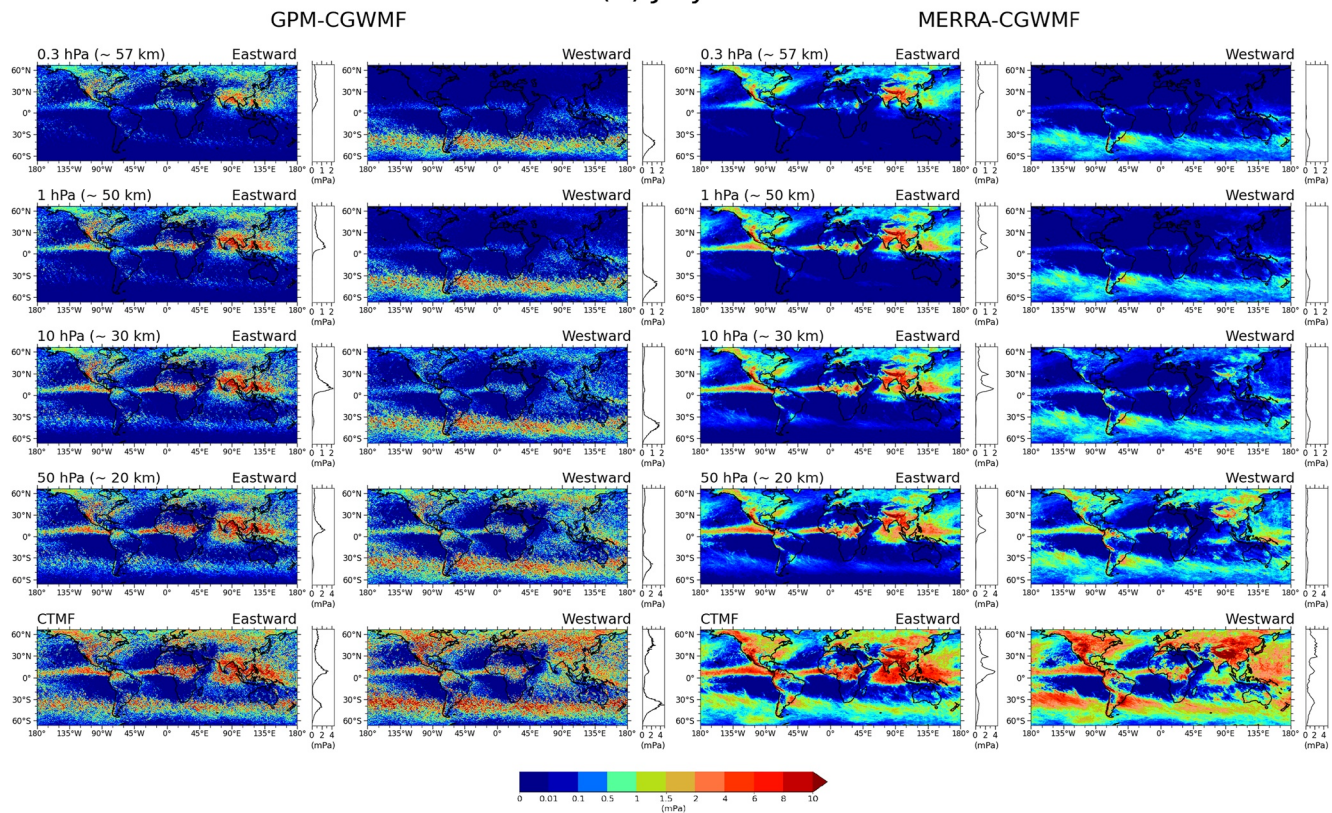


Figure 8. (Continued)

under the influence of the easterly (westerly) winds in the stratosphere, providing positive (negative) CGWD in the upper stratosphere. In the winter SH midlatitudes (30° – 60° S), where the largest difference in CTMF between GPM and MERRA-2 is present, the CGWD calculated using GPM at $z \approx 55$ km is -2.5 $\text{m s}^{-1} \text{day}^{-1}$, which is significantly smaller than the -0.6 $\text{m s}^{-1} \text{day}^{-1}$ of MERRA-2 (Figure 10b).

Figure 11 shows the 6 yr mean of the zonally averaged CGWD calculated using GPM (upper) and MERRA-2 (middle), and their differences (bottom) in January (left) and July (right). The 6 yr averaged zonal-mean zonal wind from MERRA-2 is overlaid with solid (dashed) lines representing positive (negative) values. Above the middle stratosphere, positive and negative CGWD are present in the summer and winter hemispheres, respectively, with a much clear seasonal distinction in July. The minimum value of GPM-CGWD is -4.6 $\text{m s}^{-1} \text{day}^{-1}$ at 38° S in July, which is considerably smaller than -1.4 $\text{m s}^{-1} \text{day}^{-1}$ at 47° N in January. On the other hand, the maximum values of GPM-CGWD in January and July are similar: 10.7 (8.8) $\text{m s}^{-1} \text{day}^{-1}$ at 11° S (16° N) in January (July). The maximum CGWD occurs where the eastward momentum flux is large (Figure 8), such as in Central Africa and the Maritime Continent in January and the Asian monsoon regions in July. In the winter hemisphere midlatitudes, the westward momentum flux is larger than the eastward momentum flux (Figure 8) due to the westerly background winds in the stratosphere, affording strong negative CGWD in the mesosphere over the storm track regions. Seasonal differences in CGWD are relatively weak near the equator compared with those in midlatitudes, as CGWD is more influenced by QBO and SAO (Ern et al., 2021; Pulido & Thuburn, 2008; Schirber et al., 2014).

Compared with MERRA-CGWD, both the maximum and minimum GPM-CGWDs are larger, and their difference is the largest in the SH winter near 30° – 60° S. It is likely that MERRA-CTMF, which is significantly smaller than GPM-CTMF in the SH midlatitude (30° – 60° S; Figure 7), attributes to the smaller MERRA-CGWD there. Furthermore, since a stronger spectral power of CTMF exists at high phase speed components for GPM (Figure 7) due to deeper clouds, there are more chances for the high phase-speed CGWs to propagate to the mesosphere without filtering by the background wind below. Subsequently, large amounts of drag will be deposited in the meso-

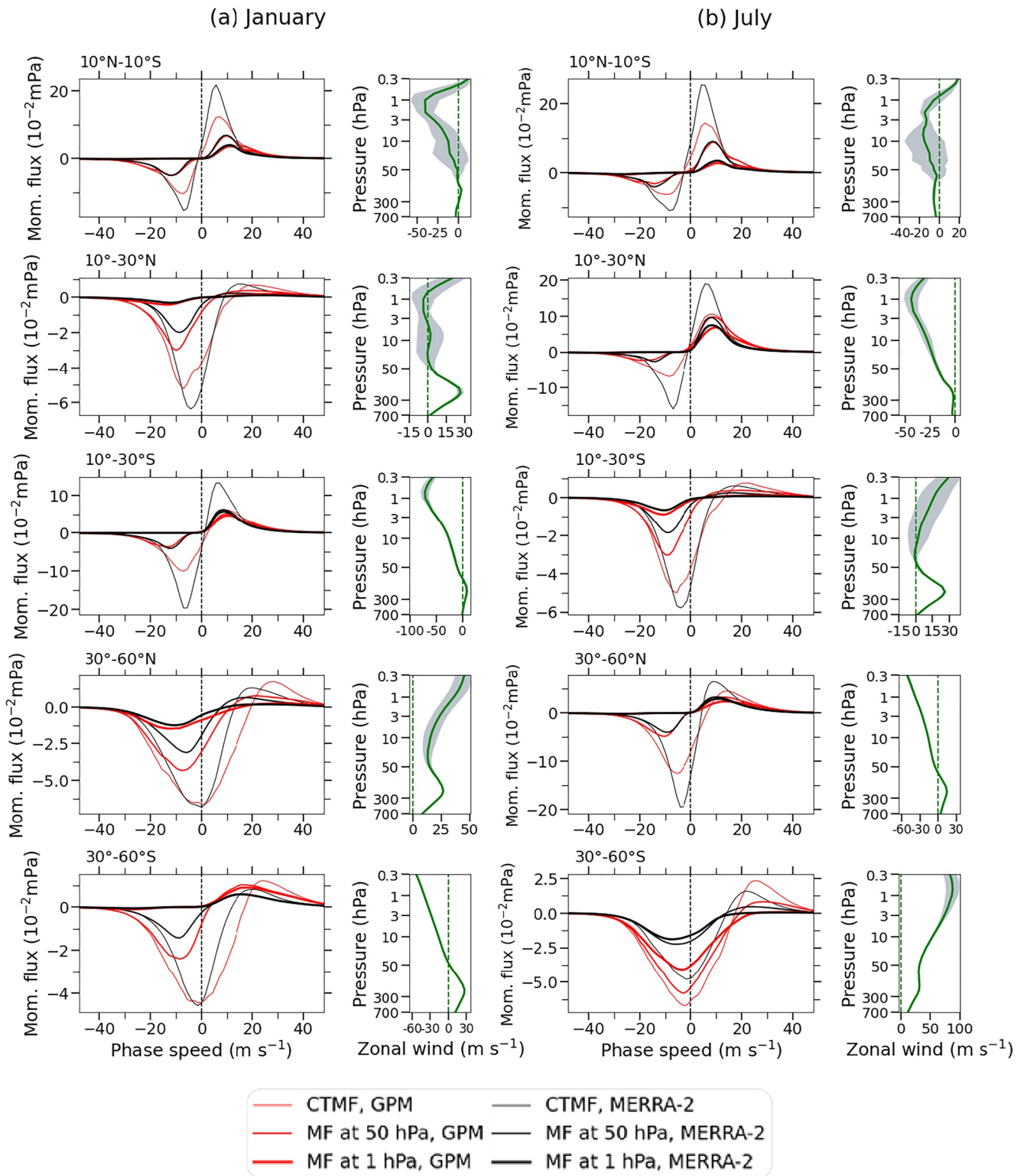


Figure 9. The 6 yr (June 2014 to May 2020) averaged convective gravity wave momentum flux (CGWMF) spectrum at three selected levels (cloud top, 50 hPa, and 1 hPa) using Global Precipitation Measurement (GPM; red) and Modern-Era Retrospective Analysis for Research and Applications, Version 2 (MERRA-2; black) averaged over 10°N–10°S, 10°–30°N, 10°–30°S, 30°–60°N, and 30°–60°S in (a) January and (b) July. Green line in the right of each plot indicates the zonal wind averaged over the same period and location. Gray-shaded area in the right of each plot denotes the standard deviation of the zonal wind.

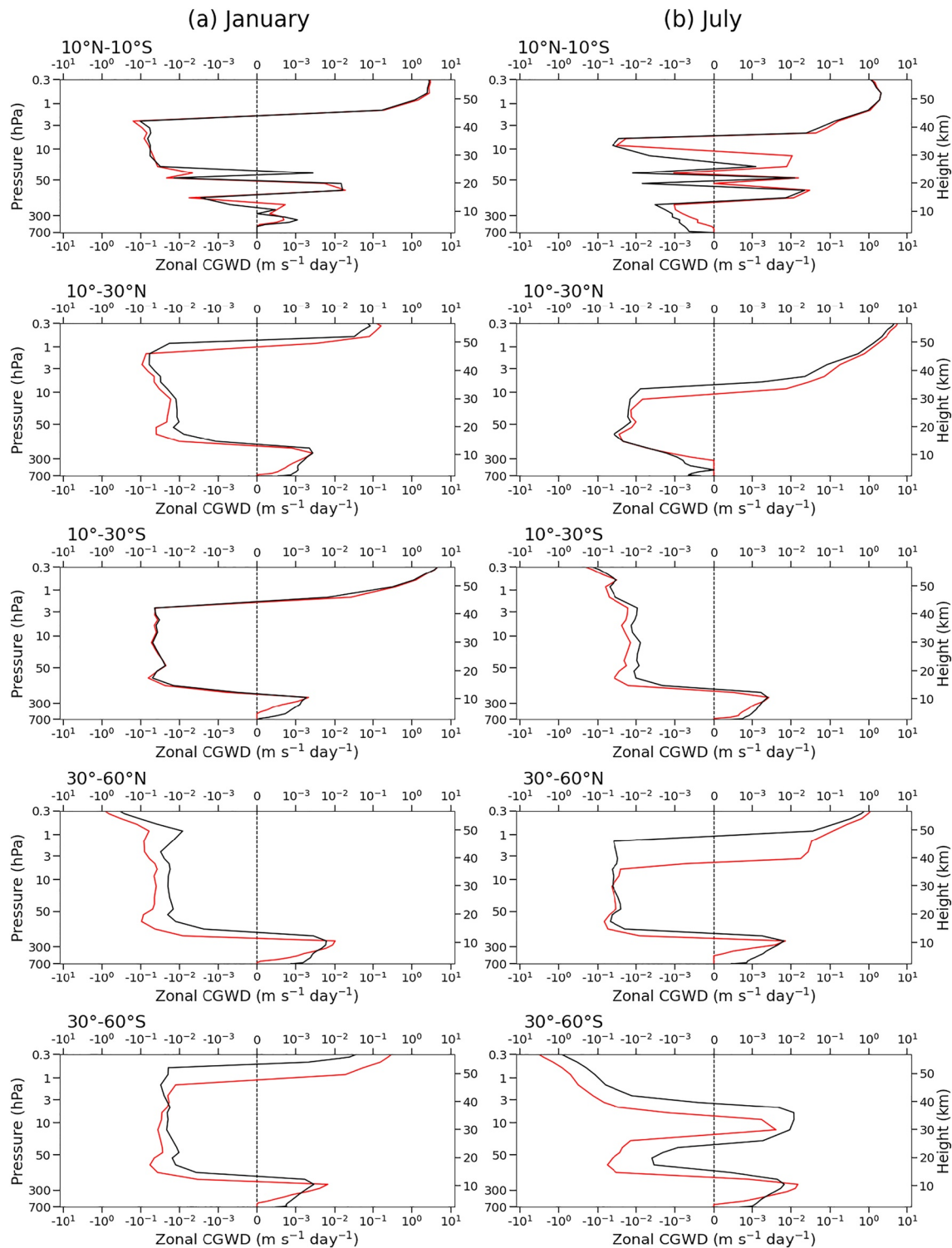


Figure 10. The 6 yr (June 2014 to May 2020) averaged zonal CGWD using Global Precipitation Measurement (GPM; red) and Modern-Era Retrospective Analysis for Research and Applications, Version 2 (MERRA-2; black) averaged over 10°N–10°S, 10°–30°N, 10°–30°S, 30°–60°N, and 30°–60°S in (a) January and (b) July.

sphere when they are broken. Since the CGWD parameterization used in this study considers the spatiotemporal variations of both convective source spectrum and WRF, it can represent more realistic variations in CGWD compared to any nonorographic parameterization assuming a constant GW source spectrum (Kang et al., 2017; Plougonven et al., 2020). However, the significant difference between GPM-CGWD and MERRA-CGWD, as

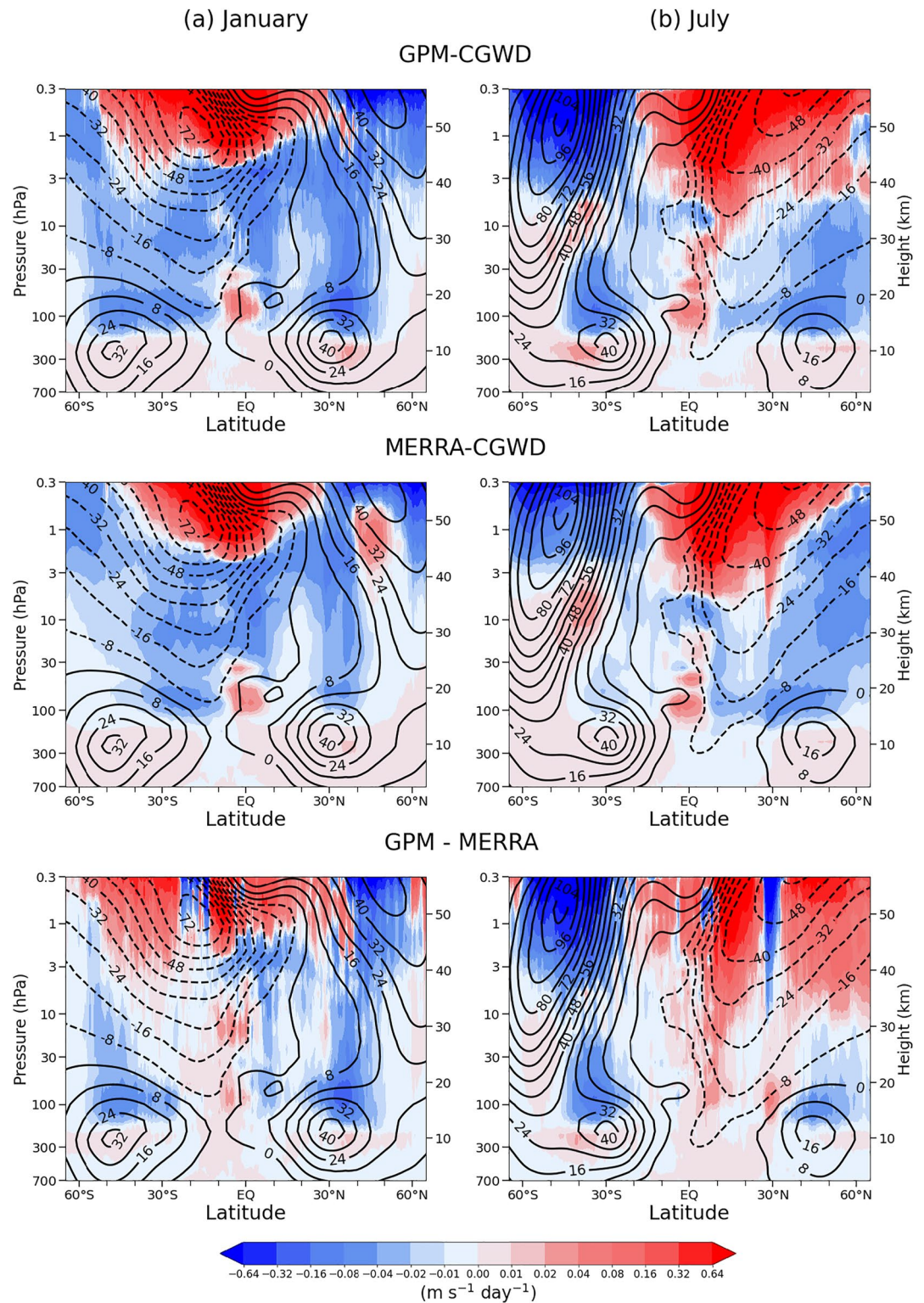


Figure 11. Latitude-height cross sections of the 6 yr (June 2014–May 2020) averaged CGWD (shading) calculated using Global Precipitation Measurement (GPM; top) and Modern-Era Retrospective Analysis for Research and Applications, Version 2 (MERRA-2; middle), and their differences (bottom) in (a) January and (b) July. Positive (negative) zonal-mean zonal winds are plotted as solid (dashed) lines, with contour intervals of 8 m s^{-1} .

revealed by the same color scales among the CGWDs by GPM, MERRA-2, and GPM-MERRA in Figure 11, demonstrates that uncertainties in the convective source information, such as CMHR and cloud top and bottom heights, afford uncertainties in the CGWD magnitude even when source-dependent CGW parameterization is implemented in GCM.

To examine the impacts of GPM-LHR on QBO, CGWD averaged between 10°N and 10°S that is calculated using GPM and MERRA-2 from June 2014 to May 2020 and their differences are shown in Figure 12. CGWD below 40 km is mainly induced by a critical-level filtering process, and positive (negative) CGWD is provided in the positive (negative) wind shear zone, which greatly contributes to the QBO descent. As is well known, negative QBO forcing by CGWs is larger than that by any equatorial waves, and positive QBO forcing by CGWs is comparable to that by Kelvin waves (Ern et al., 2014; Kang et al., 2020; Y.-H. Kim & Chun, 2015b; Pahlavan et al., 2021).

Above 40 km, positive CGWD is predominant for both GPM and MERRA-2. The difference in CGWD between GPM and MERRA-2 is evident above $z = 40$ km, with larger values for GPM than MERRA-2. At $z = 45\text{--}50$ km, the CGWD value for GPM ($19.2\text{ m s}^{-1}\text{ month}^{-1}$) is 5% larger than that for MERRA-2 ($18.4\text{ m s}^{-1}\text{ month}^{-1}$),

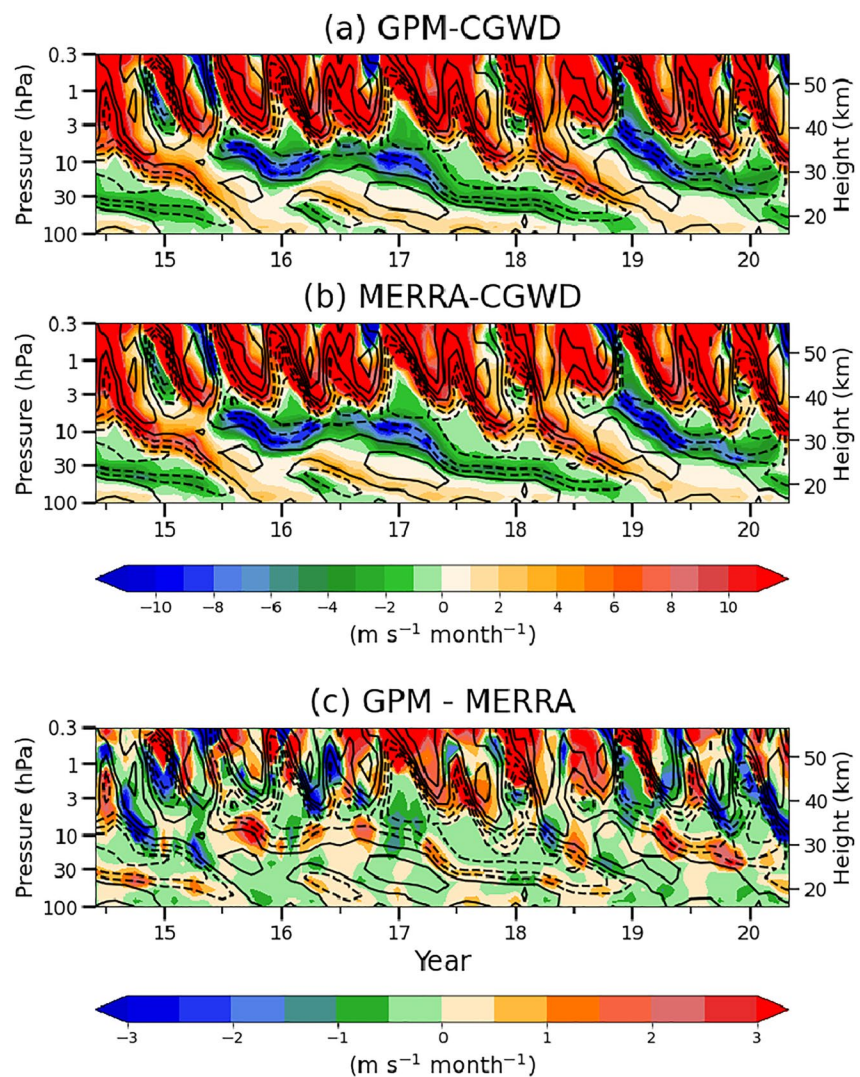


Figure 12. Time-height cross sections of the CGWD (shading) calculated using (a) Global Precipitation Measurement (GPM) and (b) Modern-Era Retrospective Analysis for Research and Applications, Version 2 (MERRA-2) from June 2014 to May 2020 averaged over 10°N–10°S, and (c) difference between (a) and (b). Positive (negative) zonal winds are plotted as solid (dashed) lines, with contour intervals of 10 m s^{-1} .

and CGWD is about 30%–70% of the forcing required to drive the equatorial SAO of 30–60 m s⁻¹ month⁻¹ in ERA-Interim, as shown in Ern et al. (2015). This result is consistent with Ern et al. (2021), who suggested that saturation of high phase speed GWs play an important role in driving the SAO. Relatively larger values of GPM-CGWD than those of MERRA-CGWD above $z = 40$ km is attributed to the relatively strong power of the eastward propagating components of CTMF at high phase speeds (Figure 9), and consequently, more eastward propagating CGWs can reach above $z = 40$ km, particularly above 1 hPa where the easterly background wind exists both in January (Figure 9a) and July (Figure 9b). On the other hand, little difference exists between CGWD calculated using GPM and MERRA-2 in the equatorial stratosphere below $z = 40$ km, where the QBO is dominant. This confirms that the CGWD during the 2015/2016 and 2019/2020 QBO disruptions (Kang & Chun, 2021; Kang et al., 2020), which is the same as MERRA-CGWD, comprises less uncertainty with respect to the heating information.

Recently, Polichtchouk et al. (2022) performed high-resolution simulations with approximate 1.4 km horizontal grid spacing for November 2018 and August 2019 using the ECMWF Integrated Forecast System. They showed that in November 2018 (August 2019), the magnitude of GWD averaged between 10°N and 10°S was maximal at 33 (17) hPa, with a contribution of 55% explained by the small-scale GWs with wavenumbers greater than 399. Figure S6 in Supporting Information S1 shows the zonal CGWD over the same period as in Polichtchouk et al. (2022). The overall vertical structure is similar to Figure 6c in Polichtchouk et al. (2022). For example, the maximum magnitude of CGWD occurs at 35 (14) hPa (Figure S6 in Supporting Information S1). This implies that the small-scale GWs in the tropical region are relatively well represented by the CGW parameterization used here. However, the magnitude of the CGWD using both GPM and MERRA-2 is approximately 1.5 times smaller than GW drag (GWD) in Polichtchouk et al. (2022). Moreover, the ratio between CGWD in the lower stratosphere (lower than ~70 hPa) and CGWD in the mid-to-upper stratosphere is smaller than that in Polichtchouk et al. (2022). The relatively small magnitude of the parameterized CGWD in the lower stratosphere compared to the explicitly resolved GWD suggests a method for updating the current GW parameterizations, which may help alleviate the common bias of the QBO amplitude in the lower stratosphere (e.g., Bushell et al., 2020).

4. Discussion

4.1. Convective-Stratiform Separation

The observed precipitation from the satellite can be classified into convective and stratiform types depending on the microphysical processes of the growth and fallout of the precipitation, which is not related to the dynamic stability or strength of the vertical motion (Houze, 1997). In detail, the rain type of the GPM dual-frequency precipitation radar (DPR) is classified as a convective cloud if no bright bands are present, while it is classified as stratiform if a localized bright band area is present (Awaka et al., 2016). Consequently, shallow clouds with low cloud top heights, wherein bright bands hardly appear, are classified as convective clouds. On the other hand, convective clouds are often classified as stratiform in the midlatitudes, where the temperature is cooler than that near the equator. Therefore, such a procedure affords uncertainty in the precise classification of convective and stratiform clouds. As an example, many precipitation areas related to typhoons Nangka (2015) and Soudelor (2015) were classified as stratiform in GPM DPR (J. Kim & Shin, 2020). This suggests that precipitations classified as stratiform clouds, accounting for most of the total precipitation in the TRMM precipitation radar and GPM DPR (Gao et al., 2017), can partly be convective clouds. Therefore, in this study, we employ GPM 3GCSH, which does not classify convective and stratiform clouds, to analyze the CMHR and CGWMF characteristics in the midlatitudes without data loss.

Recently, Liu et al. (2022) calculated CGWMF at 100 hPa using TRMM convective LHR profiles from the tropics to subtropics. Compared to their study, CGWMF in the subtropical regions is larger in the present study because stratiform type is not excluded (not shown). When we only use LHR classified as convective given by GPM 2HCSH (GPM Science Team, 2017b), the conclusions of this study do not significantly change (Figures S7 and S8 in Supporting Information S1) and only minor differences are afforded. First, the CGWMF at 50 hPa over 10°N–10°S yields a broader phase-speed spectrum than the original result. This is because strong and deep convections are selected in the tropics when the stratiform clouds are excluded, which is similar to the results of Alexander et al. (2021). Second, in July, the momentum flux using 2HCSH is smaller than that using 3GCSH in the SH midlatitudes because the stratiform fractions exceed 60% in the midlatitudes.

4.2. Cloud Top and Bottom Height

In this study, the criteria for determining the cloud top and bottom heights from the LHR profiles of GPM and MERRA-2 are adapted from Stephan and Alexander (2015) and Kang et al. (2020), respectively. In Kang et al. (2020), who calculated CGWMF and CGWD using MERRA-2 DTDTMST, the DTDTMST had a long tail structure in the upper stratosphere, unlike the LHR profiles based on the GPM satellite data, and considering this, the threshold for determining cloud top height was determined to be 20%. Stephan and Alexander (2015) defined the top of heating profiles as the level where the heating rate falls to 10% of the CMHR and the bottom as the heating where the heating rate falls to zero. They developed an algorithm to generate heating profiles using defined values and confirmed that the precipitation data could reconstruct heating profiles simulated in the cloud-resolving model. Since the LUTs were constructed by the cloud-resolving model in the GPM CSH, the top and bottom heights were defined using the same thresholds following Stephan and Alexander (2015).

As the cloud top and bottom heights are important in CTMF and the resultant CGWD, their sensitivities to thresholds to determine the cloud top and bottom heights are analyzed by an additional calculation of the GPM using the method to determine the cloud top and bottom heights applied to MERRA-2 (GPM_MERRA). In GPM_MERRA, cloud top height is decreased and cloud-bottom height is slightly increased, especially in the midlatitudes, yielding shallower clouds. The absolute CTMF in GPM_MERRA is slightly larger than the original GPM (GPM_CTL), with a similar horizontal distribution (Figure S9 in Supporting Information S1). This is likely because the shallower convection allows for stronger WFRF at low phase speeds where the convective source is stronger (Figure 7). The CGWD of the GPM_MERRA is very similar to the GPM_CTL in most latitude bins and heights (not shown), but it is slightly smaller than the GPM_CTL in the upper stratosphere, especially in 30°–60°S in July. However, CGWD by two GPM calculations is still larger than that by the MERRA-2 (Figure 10), implying that applying different thresholds for the cloud top and bottom heights to GPM does not significantly change the results of the current study, at least for the period considered in the present study.

4.3. Comparison With TRMM Products

In the present study, we compared the GPM results to the MERRA-2. In order to make sure the reality of the GPM results, the comparison between CGWMF and CGWD from GPM and those from TRMM is made additionally. The data set used is the TRMM 3GCSH. Since TRMM 3GCSH only covers 37°N–37°S, comparisons are conducted for tropical and subtropic regions. After October 2014, the precipitation radar of the TRMM could not obtain normal observations due to orbital descent (Takahashi et al., 2016), and therefore TRMM data for four months from June–September 2014 are used for the comparison.

Figure 13 represents the 4 months averaged (a) CTMF spectrum and (b) CGWD using GPM (red), TRMM (green), and MERRA-2 (black) over three latitudinal bins (10°N–10°S, 10°–30°N, and 10°–30°S). First, the CTMF spectrum (Figure 13a) calculated using the TRMM at high (low) phase speeds is larger (smaller) than that using MERRA-2, which is consistent with the original results using the GPM. Although the momentum flux of the TRMM is slightly smaller than that of the GPM at low phase speeds, momentum fluxes at high phase speeds are very similar to each other. When carefully examined the convective source and WFRF spectra (Figure S10 in Supporting Information S1), it is found that the WFRF of the GPM is slightly larger than that of the TRMM at low phase speeds, while the convective source spectrum is similar. This is likely because the GPM detects shallow convection better than TRMM (Lang & Tao, 2018). Second, vertical structure of the CGWD (Figure 13b) calculated using the GPM and TRMM is similar to each other, although the CGWD by the TRMM is slightly smaller than either by the GPM or MERRA-2 in 10°–30°S in the upper stratosphere. The above results support that the differences in the CTMF and CGWD between the GPM and MERRA-2 shown in the present study are likely robust without significant differences depending on the type of the satellite data used. This implies that more realistic cloud information is required in GCMs, when convective source-based CGWD parameterization is implemented, for better representation of CGWMF and CGWD.

5. Summary and Conclusions

In this paper, the spatiotemporal characteristics of LHR from GPM 3GCSH were investigated for the period from June 2014 to May 2020, and CGWMF and CGWD using the GPM LHR were calculated and compared with those

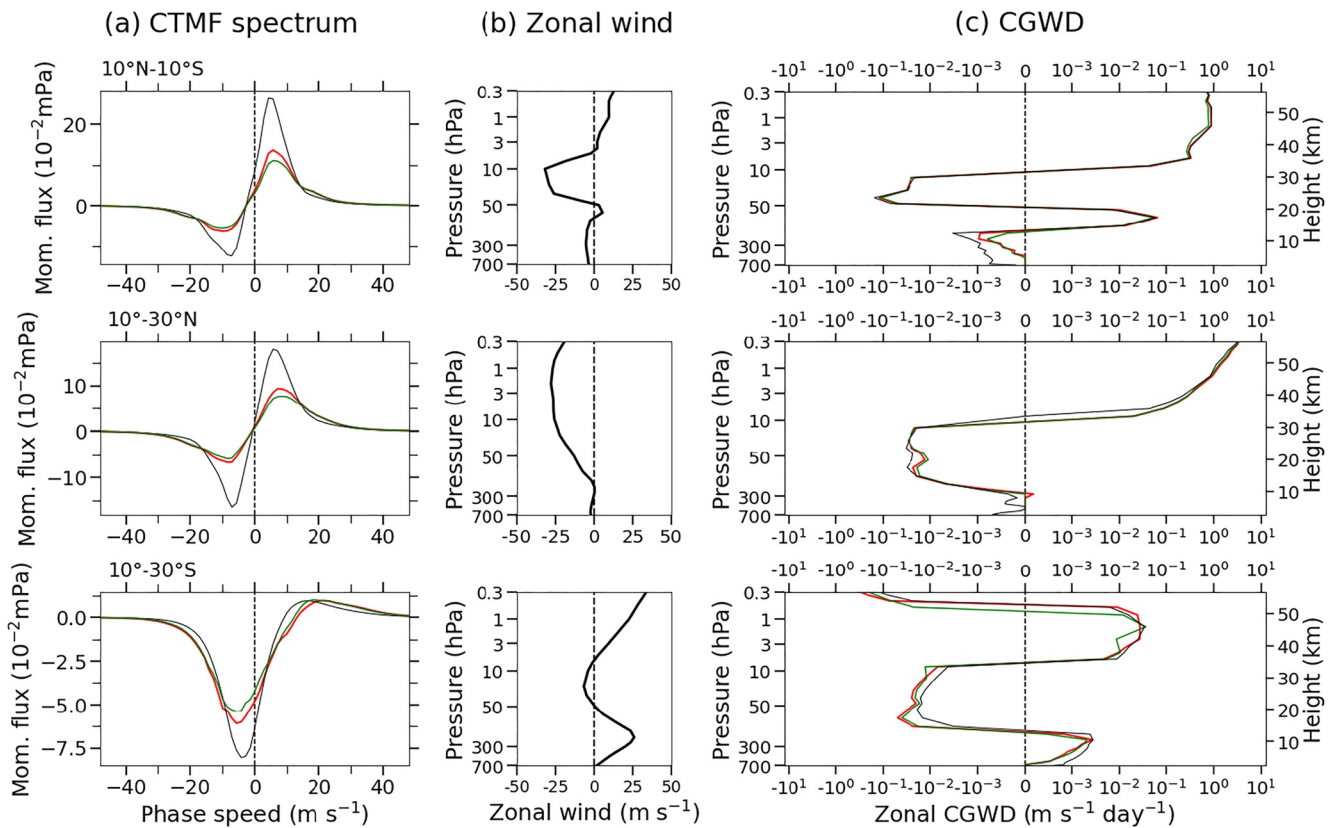


Figure 13. The (a) cloud-top momentum flux (CTMF) spectrum, (b) zonal wind, and (c) CGWD profiles averaged for 4 months (June–September 2014) calculated using the Global Precipitation Measurement (GPM; red), Tropical Rainfall Measuring Mission (TRMM; green), and Modern-Era Retrospective Analysis for Research and Applications, Version 2 (MERRA-2; black) data over each latitudinal bin.

using the MERRA-2 LHR. The GPM-LHR profile exhibited a bimodal structure near the equator but a unimodal structure in the other regions. In the tropical regions, the maximum LHR located at $z = 6$ km and the secondary maximum appeared at $z = 2$ km. The averaged CMHR was maximal between 10°N and 10°S . Additionally, the magnitude and temporal variations of CMHR were similar between GPM and MERRA-2. The largest difference in CMHR between GPM and MERRA-2 was found over land, where the CMHR of MERRA-2 was larger than that of GPM. The correlation coefficient between GPM LHR and MERRA-2 LHR ranged between 0.43 and 0.96, with the lowest in the NH midlatitude ($30^\circ\text{--}60^\circ\text{N}$).

The CTMF was maximum in the storm track regions for both GPM-CTMF and MERRA-CTMF, although the maximum CMHR occurred near the equator. This is due to that the CTMF was determined by a spectral combination of the convective source, represented by CMHR, and WFRF, which represents the critical-level filtering and resonance between vertical harmonics of the convective source and natural wave modes. The overlap between CMHR and WFRF was the maximal in the storm tracks. Additionally, the nonlinearity effect of CGWs included in the CTMF formulation was the largest in the equatorial region where the convective activities are strong, which reduced the CTMF magnitude. Relative to MERRA-CTMF, GPM-CTMF was enhanced in the SH midlatitudes in July by a factor of 1.7. In this region, strong convective events occurred more frequently in GPM than in MERRA-2, yielding stronger GPM-CTMF, which is in contrast to CMHR. At the cloud top, the eastward momentum flux was larger than the westward momentum flux in the low latitudes, while the opposite was true in the midlatitudes.

The characteristics and spatial distributions of CGWMF and CGWD at levels above the cloud top were investigated by assuming the columnar vertical propagation based on Lindzen's saturation theory. In January, the maximum of the westward momentum flux was located in the NH hemisphere, and it gradually dissipated from 50 to 0.3 hPa, providing negative CGWD in the winter stratosphere. The CGWMF near the equatorial region was less filtered than in the midlatitudes from the cloud top to the lower stratosphere due to the weak easterly winds

there. The CGWMF of GPM above the cloud top in the storm track regions (30° – 60°) was greater in July than in January, which is much larger than that of MERRA-2 in July. Generally, above the middle stratosphere, the CGWD in the summer hemisphere was positive, while the CGWD in the winter hemisphere was negative. The maximum and minimum values of the GPM-CGWD were larger than those of MERRA-CGWD. Particularly, the magnitude of GPM-CGWD in the SH was very large compared to that of MERRA-CGWD. In the equatorial region, positive CGWD was dominant above $z = 40$ km in both GPM and MERRA-2, and the magnitude was larger in GPM-CGWD than that in MERRA-CGWD. Below $z = 40$ km, positive (negative) CGWD was afforded in the positive (negative) wind shear zone, contributing to the QBO descent. Little difference existed in CGWD between GPM and MERRA-2 below $z = 40$ km, implying that the estimated CGWD during the two QBO disruptions by Kang and Chun (2021) and Kang et al. (2020) using MERRA-2 is quite reasonable.

Convective heating profiles are important information for not only the CGW parameterization but also other atmospheric phenomena, such as Hadley circulation (Fierro et al., 2009), MJO (Li et al., 2009), and Asian monsoon (Choudhury & Krishnan, 2011; Jin et al., 2013). This study showed that the monthly mean convective heating rates in modern reanalysis are quite realistic in terms of zonal-mean climatology and monthly to inter-annual variabilities, especially in the equatorial region. This affords relatively small differences in the CGWD in the equatorial region between MERRA-2 and GPM. Although the GPM estimated LHR are based on the high-resolution modeling due to the difficulty in direct observations, such a retrieval should be continued to enhance our understanding and representation of convective heating. Particularly, efforts should be made for better quantifying the convective heating rates in the midlatitudes that still exhibit large uncertainties.

Appendix A: List of Abbreviations

Table A1

| Table A1 <i>List of Abbreviations Used in the Paper</i> | |
|--|--|
| Abbreviation | Definition |
| CFSR | Climate Forecast System Reanalysis |
| CGW | Convective gravity wave |
| CGWD | Convective gravity wave drag |
| CGWMF | Convective gravity wave momentum flux |
| CMHR | Column-maximum heating rate |
| CSH | Convective-stratiform heating |
| CTMF | Cloud top momentum flux |
| DJF | December–January–February |
| DPR | Dual-frequency precipitation radar |
| ERA5 | ECMWF Reanalysis v5 |
| GCM | General circulation model |
| GPM | Global Precipitation Measurement |
| GW | Gravity wave |
| GWD | Gravity wave drag |
| HH | Hydrometeor heating |
| ITCZ | Intertropical convergence zone |
| JJA | June–July–August |
| LHR | Latent heating rate |
| LUT | Lookup table |
| MERRA-2 | Modern-Era Retrospective Analysis for Research and Applications, Version 2 |
| MHH | Maximum heating height |
| MJO | Madden-Julian oscillation |

Table A1
Continued

| Abbreviation | Definition |
|--------------|-------------------------------------|
| NH | Northern Hemisphere |
| PSD | Power spectral density |
| QBO | Quasi-biennial oscillation |
| SAO | Semi-annual oscillation |
| SH | Southern Hemisphere |
| TRMM | Tropical Rainfall Measuring Mission |
| WFRF | Wave-filtering and resonance factor |

Data Availability Statement

The MERRA-2 data (GMAO, 2015) was downloaded from the Goddard Earth Sciences Data and Information Services Center (GES DISC). The GPM 3GCSH (GPM Science Team, 2017a) was downloaded from the Goddard Earth Sciences Data and Information Services Center (GES DISC). The GPM 2HCSH (GPM Science Team, 2017b) was downloaded from the Goddard Earth Sciences Data and Information Services Center (GES DISC). The TRMM 3GCSH (TRMM, 2019) was downloaded from the Goddard Earth Sciences Data and Information Services Center (GES DISC). The ERA5 data (Hersbach et al., 2018) was downloaded from the Copernicus Climate Change Service (C3S) Climate Data Store (CDS).

Acknowledgments

This work has supported by the National Research Foundation of Korea (NRF) through a grant funded by the Korean government (MSIT) (no. 2020R1A4A1016537). This research was also supported by the Yonsei Signature Research Cluster Program of 2021 (2021-22-0003).

References

- Alexander, M. J., & Dunkerton, T. J. (1999). A spectral parameterization of mean-flow forcing due to breaking gravity waves. *Journal of the Atmospheric Sciences*, 56(24), 4167–4182. [https://doi.org/10.1175/1520-0469\(1999\)056<4167:ASPOMF>2.0.CO;2](https://doi.org/10.1175/1520-0469(1999)056<4167:ASPOMF>2.0.CO;2)
- Alexander, M. J., Liu, C. C., Bacmeister, J., Bramberger, M., Hertzog, A., & Richter, J. H. (2021). Observational validation of parameterized gravity waves from tropical convection in the Whole Atmosphere Community Climate Model. *Journal of Geophysical Research: Atmospheres*, 126, e2020JD033954. <https://doi.org/10.1029/2020JD033954>
- Awaka, J., Le, M., Chandrasekar, V., Yoshida, N., Higashiawatoko, T., Kubota, T., & Iguchi, T. (2016). Rain type classification algorithm module for GPM dual-frequency precipitation radar. *Journal of Atmospheric and Oceanic Technology*, 33(9), 1887–1898. <https://doi.org/10.1175/JTECH-D-16-0016.1>
- Beres, J. H., Alexander, M. J., & Holton, J. R. (2004). A method of specifying the gravity wave spectrum above convection based on latent heating properties and background wind. *Journal of the Atmospheric Sciences*, 61(3), 324–337. [https://doi.org/10.1175/1520-0469\(2004\)061<0324:AMOSTG>2.0.CO;2](https://doi.org/10.1175/1520-0469(2004)061<0324:AMOSTG>2.0.CO;2)
- Bosilovich, M. G., Lucchesi, R., & Suarez, M. (2016). MERRA-2: File specification GMAO Office Note No. 9 (Version 1.1).
- Bushell, A. C., Anstey, J. A., Butchart, N., Kawatani, Y., Osprey, S. M., & Richter, J. H. (2020). Evaluation of the Quasi-Biennial Oscillation in global climate models for the SPARC QBO-initiative. *Quarterly Journal of the Royal Meteorological Society*, 148, 1459–1489. <https://doi.org/10.1002/qj.3765>
- Choi, H.-J., & Chun, H.-Y. (2011). Momentum flux spectrum of convective gravity waves. Part I: An update of a parameterization using mesoscale simulations. *Journal of the Atmospheric Sciences*, 68(4), 739–759. <https://doi.org/10.1175/2010JAS3552.1>
- Choi, H.-J., & Chun, H.-Y. (2013). Effects of convective gravity wave drag in the Southern Hemisphere winter stratosphere. *Journal of the Atmospheric Sciences*, 70(7), 2120–2136. <https://doi.org/10.1175/JAS-D-12-0238.1>
- Choudhury, A. D., & Krishnan, R. (2011). Dynamical response of the South Asian monsoon trough to latent heating from stratiform and convective precipitation. *Journal of the Atmospheric Sciences*, 68(6), 1347–1363. <https://doi.org/10.1175/2011JAS3705.1>
- Chun, H.-Y., Choi, H.-J., & Song, I.-S. (2008). Effects of nonlinearity on convectively forced internal gravity waves: Application to a gravity wave drag parameterization. *Journal of the Atmospheric Sciences*, 65(2), 557–575. <https://doi.org/10.1175/2007JAS2255.1>
- Corcos, M., Hertzog, A., Plougonven, R., & Podglajen, A. (2021). Observation of gravity waves at the tropical tropopause using superpressure balloons. *Journal of Geophysical Research: Atmospheres*, 126, e2021JD035165. <https://doi.org/10.1029/2021JD035165>
- Cui, W., Dong, X., Xi, B., & Kennedy, A. (2017). Evaluation of reanalyzed precipitation variability and trends using the gridded gauge-based analysis over the CONUS. *Journal of Hydrometeorology*, 18(8), 2227–2248. <https://doi.org/10.1175/JHM-D-17-0029.1>
- Eckermann, S. D., Doyle, J. D., Reinecke, P. A., Reynolds, C. A., Smith, R. B., Fritts, D. C., & Dörnbrack, A. (2019). Stratospheric gravity wave products from satellite infrared nadir radiances in the planning, execution, and validation of aircraft measurements during DEEPWAVE. *Journal of Applied Meteorology and Climatology*, 58(9), 2049–2075. <https://doi.org/10.1175/JAMC-D-19-0015.1>
- Emori, S., Hasegawa, A., Suzuki, T., & Dairaku, K. (2005). Validation, parameterization dependence, and future projection of daily precipitation simulated with a high-resolution atmospheric GCM. *Geophysical Research Letters*, 32. <https://doi.org/10.1029/2004GL022306>
- Ern, M., Diallo, M., Preusse, P., Mlyneczek, M. G., Schwartz, M. J., Wu, Q., & Riese, M. (2021). The semiannual oscillation (SAO) in the tropical middle atmosphere and its gravity wave driving in reanalyses and satellite observations. *Atmospheric Chemistry and Physics*, 21, 13763–13795. <https://doi.org/10.5194/acp-21-13763-2021>
- Ern, M., Ploeger, F., Preusse, P., Gille, J. C., Gray, L. J., Kalisch, S., et al. (2014). Interaction of gravity waves with the QBO: A satellite perspective. *Journal of Geophysical Research*, 119, 2329–2355. <https://doi.org/10.1002/2013JD020731>

- Ern, M., Preusse, P., Gille, J. C., Hepplewhite, C. L., Mlynczak, M. G., Russell, J. M., & Riese, M. (2011). Implications for atmospheric dynamics derived from global observations of gravity wave momentum flux in stratosphere and mesosphere. *Journal of Geophysical Research: Atmospheres*, *116*. <https://doi.org/10.1029/2011JD015821>
- Ern, M., Preusse, P., & Riese, M. (2015). Driving of the SAO by gravity waves as observed from satellite. *Annales Geophysicae*, *33*, 483–504. <https://doi.org/10.5194/angeo-33-483-2015>
- Fierro, A. O., Simpson, J., LeMone, M. A., Straka, J. M., & Smull, B. F. (2009). On how hot towers fuel the Hadley cell: An observational and modeling study of line-organized convection in the equatorial trough from TOGA COARE. *Journal of the Atmospheric Sciences*, *66*(9), 2730–2746. <https://doi.org/10.1175/2009JAS3017.1>
- Gao, J., Tang, G., & Hong, Y. (2017). Similarities and improvements of GPM dual-frequency precipitation radar (DPR) upon TRMM precipitation radar (PR) in global precipitation rate estimation, type classification, and vertical profiling. *Remote Sensing*, *9*(11), 1142. <https://doi.org/10.3390/rs9111142>
- Gelaro, R., McCarty, W., Suárez, M. J., Todling, R., Molod, A., Takacs, L., et al. (2017). The Modern-Era Retrospective Analysis for Research and Applications, Version 2 (MERRA-2). *Journal of Climate*, *30*, 5419–5454. <https://doi.org/10.1175/JCLI-D-16-0758.1>
- Global Modeling and Assimilation Office (GMAO). (2015). MERRA-2 inst3_3d_asm_Np: 3d, 3-Hourly, Instantaneous, Pressure-Level, Assimilation, Assimilated Meteorological Fields V5.12.4 [Dataset]. Goddard Earth Sciences Data and Information Services Center (GES DISC). <https://doi.org/10.5067/QBZ6MG944HW0>
- GPM Science Team. (2017a). GPM DPR (Gridded Convective Stratiform Heating) L3 1.5 hr 0.5° × 0.5° V06 [Dataset]. Goddard Earth Sciences Data and Information Services Center (GES DISC). <https://doi.org/10.5067/GPM/DPRGMI/CSH/3G/06>
- GPM Science Team. (2017b). GPM DPR and GMI Combined Stratiform Heating L2 1.5 hr 5 km V06 [Dataset]. Goddard Earth Sciences Data and Information Services Center (GES DISC). <https://doi.org/10.5067/GPM/DPRGMI/CSH/2H/06>
- Hersbach, H., Bell, B., Berrisford, P., Biavati, G., Horányi, A., Muñoz Sabater, J., et al. (2018). ERA5 hourly data on pressure levels from 1959 to present [Dataset]. Copernicus Climate Change Service (C3S) Climate Data Store (CDS). <https://doi.org/10.24381/cds.bd0915c6>
- Hersbach, H., Bell, B., Berrisford, P., Hirahara, S., Horányi, A., Muñoz-Sabater, J., et al. (2020). The ERA5 global reanalysis. *Quarterly Journal of the Royal Meteorological Society*, *146*, 1999–2049. <https://doi.org/10.1002/qj.3803>
- Hindley, N. P., Wright, C. J., Smith, N. D., & Mitchell, N. J. (2015). The southern stratospheric gravity wave hot spot: Individual waves and their momentum fluxes measured by COSMIC GPS-RO. *Atmospheric Chemistry and Physics*, *15*, 7797–7818. <https://doi.org/10.5194/acp-15-7797-2015>
- Hocke, K., Lainer, M., Moreira, L., Hagen, J., Fernandez Vidal, S., & Schranz, F. (2016). Atmospheric inertia-gravity waves retrieved from level-2 data of the satellite microwave limb sounder Aura/MLS. *Annales Geophysicae*, *34*, 781–788. <https://doi.org/10.5194/angeo-34-781-2016>
- Hoffmann, L., Grimsdell, A. W., & Alexander, M. J. (2016). Stratospheric gravity waves at Southern Hemisphere orographic hotspots: 2003–2014 AIRS/Aqua observations. *Atmospheric Chemistry and Physics*, *16*, 9381–9397. <https://doi.org/10.5194/acp-16-9381-2016>
- Hoffmann, L., Xue, X., & Alexander, M. J. (2013). A global view of stratospheric gravity wave hotspots located with Atmospheric Infrared Sounder observations. *Journal of Geophysical Research: Atmospheres*, *118*, 416–434. <https://doi.org/10.1029/2012JD018658>
- Holt, L. A., Lott, F., Garcia, R. R., Kiladis, G. N., Cheng, Y. M., Anstey, J. A., et al. (2020). An evaluation of tropical waves and wave forcing of the QBO in the QBOi models. *Quarterly Journal of the Royal Meteorological Society*, *148*, 1541–1567. <https://doi.org/10.1002/qj.3827>
- Hou, A. Y., Kakar, R. K., Neeck, S., Azarbarzin, A. A., Kummerow, C. D., Kojima, M., et al. (2014). The Global Precipitation Measurement mission. *Bulletin of the American Meteorological Society*, *95*(5), 701–722. <https://doi.org/10.1175/BAMS-D-13-00164.1>
- Houze, R. A. (1997). Stratiform precipitation in regions of convection: A meteorological paradox? *Bulletin of the American Meteorological Society*, *78*(10), 2179–2196. [https://doi.org/10.1175/1520-0477\(1997\)078<2179:SPIROC>2.0.CO;2](https://doi.org/10.1175/1520-0477(1997)078<2179:SPIROC>2.0.CO;2)
- Huaman, L., & Schumacher, C. (2018). Assessing the vertical latent heating structure of the east Pacific ITCZ using the CloudSat CPR and TRMM PR. *Journal of Climate*, *31*(7), 2563–2577. <https://doi.org/10.1175/JCLI-D-17-0590.1>
- Jalihal, C., Bosmans, J. H. C., Srinivasan, J., & Chakraborty, A. (2019). The response of tropical precipitation to Earth's precession: The role of energy fluxes and vertical stability. *Climate of the Past*, *15*, 449–462. <https://doi.org/10.5194/cp-15-449-2019>
- Jewtoukoff, V., Plougonven, R., & Hertzog, A. (2013). Gravity waves generated by deep tropical convection: Estimates from balloon observations and mesoscale simulations. *Journal of Geophysical Research: Atmospheres*, *118*, 9690–9707. <https://doi.org/10.1002/jgrd.50781>
- Jiang, X., Waliser, D. E., Olson, W. S., Tao, W.-K., L'Ecuyer, T. S., Li, K. F., et al. (2011). Vertical diabatic heating structure of the MJO: Intercomparison between recent reanalyses and TRMM estimates. *Monthly Weather Review*, *139*(10), 3208–3223. <https://doi.org/10.1175/2011MWR3636.1>
- Jin, Q., Yang, X. Q., Sun, X. G., & Fang, J. B. (2013). East Asian summer monsoon circulation structure controlled by feedback of condensational heating. *Climate Dynamics*, *41*, 1885–1897. <https://doi.org/10.1007/s00382-012-1620-9>
- Kalisch, S., Chun, H.-Y., Ern, M., Preusse, P., Trinh, Q. T., Eckermann, S. D., & Riese, M. (2016). Comparison of simulated and observed convective gravity waves. *Journal of Geophysical Research: Atmospheres*, *121*, 13474–13492. <https://doi.org/10.1002/2016JD025235>
- Kang, M.-J., & Chun, H.-Y. (2021). Contributions of equatorial waves and small-scale convective gravity waves to the 2019/2020 quasi-biennial oscillation (QBO) disruption. *Atmospheric Chemistry and Physics*, *21*, 9839–9857. <https://doi.org/10.5194/acp-21-9839-2021>
- Kang, M.-J., Chun, H.-Y., & Garcia, R. R. (2020). Role of equatorial waves and convective gravity waves in the 2015/2016 quasi-biennial oscillation disruption. *Atmospheric Chemistry and Physics*, *20*, 14669–14693. <https://doi.org/10.5194/acp-20-14669-2020>
- Kang, M.-J., Chun, H.-Y., & Kim, Y.-H. (2017). Momentum flux of convective gravity waves derived from an offline gravity wave parameterization. Part I: Spatiotemporal variations at source level. *Journal of the Atmospheric Sciences*, *74*(10), 3167–3189. <https://doi.org/10.1175/JAS-D-17-0053.1>
- Kang, M.-J., Chun, H.-Y., Kim, Y.-H., Preusse, P., & Ern, M. (2018). Momentum flux of convective gravity waves derived from an offline gravity wave parameterization. Part II: Impacts on the quasi-biennial oscillation. *Journal of the Atmospheric Sciences*, *75*(11), 3753–3775. <https://doi.org/10.1175/JAS-D-18-0094.1>
- Kawatani, Y., Watanabe, S., Sato, K., Dunkerton, T. J., Miyahara, S., & Takahashi, M. (2010). The roles of equatorial trapped waves and internal inertia-gravity waves in driving the quasi-biennial oscillation. Part I: Zonal mean wave forcing. *Journal of the Atmospheric Sciences*, *67*(4), 963–980. <https://doi.org/10.1175/2009JAS3222.1>
- Kim, J., & Shin, D. B. (2020). A comparative study of rain/no-rain classification results using PCT from GPM/GMI data by precipitation type. *IEEE Transactions on Geoscience and Remote Sensing*, *58*(12), 8541–8554. <https://doi.org/10.1109/TGRS.2020.2988597>
- Kim, J.-E., & Alexander, M. J. (2013). Tropical precipitation variability and convectively coupled equatorial waves on submonthly time scales in reanalyses and TRMM. *Journal of Climate*, *26*(10), 3013–3030. <https://doi.org/10.1175/JCLI-D-12-00353.1>
- Kim, Y.-H., Bushell, A. C., Jackson, D. R., & Chun, H.-Y. (2013). Impacts of introducing a convective gravity-wave parameterization upon the QBO in the Met Office Unified Model. *Geophysical Research Letters*, *40*, 1873–1877. <https://doi.org/10.1002/grl.50353>

- Kim, Y.-H., & Chun, H.-Y. (2015a). Contributions of equatorial wave modes and parameterized gravity waves to the tropical QBO in HadGEM2. *Journal of Geophysical Research: Atmospheres*, *120*, 1065–1090. <https://doi.org/10.1002/2014JD022174>
- Kim, Y.-H., & Chun, H.-Y. (2015b). Momentum forcing of the quasi-biennial oscillation by equatorial waves in recent reanalyses. *Atmospheric Chemistry and Physics*, *15*, 6577–6587. <https://doi.org/10.5194/acp-15-6577-2015>
- Kim, Y.-J., Eckermann, S. D., & Chun, H.-Y. (2003). An overview of the past, present, and future of gravity-wave drag parametrization for numerical climate and weather prediction models. *Atmosphere-Ocean*, *41*(1), 65–98. <https://doi.org/10.3137/ao.410105>
- Lang, S. E., & Tao, W.-K. (2018). The next-generation Goddard convective-stratiform heating algorithm: New tropical and warm-season retrievals for GPM. *Journal of Climate*, *31*(15), 5997–6026. <https://doi.org/10.1175/JCLI-D-17-0224.1>
- Lee, J.-H., Kang, M.-J., & Chun, H.-Y. (2019). Differences in the tropical convective activities at the opposite phases of the quasi-biennial oscillation. *Asia-Pacific Journal of Atmospheric Sciences*, *55*, 317–336. <https://doi.org/10.1007/s13143-018-0096-x>
- Li, C., Jia, X., Ling, J., Zhou, W., & Zhang, C. (2009). Sensitivity of MJO simulations to diabatic heating profiles. *Climate Dynamics*, *32*, 167–187. <https://doi.org/10.1007/s00382-008-0455-x>
- Liess, S., & Geller, M. A. (2012). On the relationship between QBO and distribution of tropical deep convection. *Journal of Geophysical Research: Atmospheres*, *117*, 1–12. <https://doi.org/10.1029/2011JD016317>
- Lin, J. L., Kiladis, G. N., Mapes, B. E., Weickmann, K. M., Sperber, K. R., Lin, W., et al. (2006). Tropical intraseasonal variability in 14 IPCC AR4 climate models. Part I: Convective signals. *Journal of Climate*, *19*(12), 2665–2690. <https://doi.org/10.1175/JCLI3735.1>
- Lindzen, R. S. (1981). Turbulence and stress owing to gravity wave and tidal breakdown. *Journal of Geophysical Research: Oceans*, *86*, 9707–9714. <https://doi.org/10.1029/JC086iC10p09707>
- Liu, C., Alexander, J., Richter, J., & Baumeister, J. (2022). Using TRMM latent heat as a source to estimate convection induced gravity wave momentum flux in the lower stratosphere. *Journal of Geophysical Research: Atmospheres*, *127*, e2021JD035785. <https://doi.org/10.1029/2021JD035785>
- Mitchell, T. P., & Wallace, J. M. (1992). The annual cycle in equatorial convection and sea surface temperature. *Journal of Climate*, *5*(10), 1140–1156. [https://doi.org/10.1175/1520-0442\(1992\)005<1140:TACIEC>2.0.CO;2](https://doi.org/10.1175/1520-0442(1992)005<1140:TACIEC>2.0.CO;2)
- Newman, P. A., Coy, L., Pawson, S., & Lait, L. R. (2016). The anomalous change in the QBO in 2015–2016. *Geophysical Research Letters*, *43*, 8791–8797. <https://doi.org/10.1002/2016GL070373>
- Osprey, S. M., Butchart, N., Knight, J. R., Scaife, A. A., Hamilton, K., Anstey, J. A., et al. (2016). An unexpected disruption of the atmospheric quasi-biennial oscillation. *Science*, *353*(6306), 1424–1427. <https://doi.org/10.1126/science.aah4156>
- Pahlavan, H. A., Wallace, J. M., Fu, Q., & Kiladis, G. N. (2021). Revisiting the quasi-biennial oscillation as seen in ERA5. Part II: Evaluation of laves and wave forcing. *Journal of the Atmospheric Sciences*, *78*(3), 693–707. <https://doi.org/10.1175/JAS-D-20-0249.1>
- Plougonven, R., Cámara, A., Hertzog, A., & Lott, F. (2020). How does knowledge of atmospheric gravity waves guide their parameterizations? *Quarterly Journal of the Royal Meteorological Society*, *146*, 1529–1543. <https://doi.org/10.1002/qj.3732>
- Polichtchouk, I., Wedi, N., & Kim, Y.-H. (2022). Resolved gravity waves in the tropical stratosphere: Impact of horizontal resolution and deep convection parameterization. *Quarterly Journal of the Royal Meteorological Society*, *148*(742), 233–251. <https://doi.org/10.1002/qj.4202>
- Prakash, S., Gairola, R. M., & Mitra, A. K. (2015). Comparison of large-scale global land precipitation from multisatellite and reanalysis products with gauge-based GPCC data sets. *Theoretical and Applied Climatology*, *121*, 303–317. <https://doi.org/10.1007/s00704-014-1245-5>
- Pulido, M., & Thuburn, J. (2008). The seasonal cycle of gravity wave drag in the middle atmosphere. *Journal of Climate*, *21*(18), 4664–4679. <https://doi.org/10.1175/2008JCLI2006.1>
- Ricciardulli, L., & Garcia, R. R. (2000). The excitation of equatorial waves by deep convection in the NCAR Community Climate Model (CCM3). *Journal of the Atmospheric Sciences*, *57*(21), 3461–3487. [https://doi.org/10.1175/1520-0469\(2000\)057<3461:TEOWEB>2.0.CO;2](https://doi.org/10.1175/1520-0469(2000)057<3461:TEOWEB>2.0.CO;2)
- Saha, S., Moorthi, S., Pan, H. L., Wu, X., Wang, J., Nadiga, S., et al. (2010). The NCEP climate forecast system reanalysis. *Bulletin of the American Meteorological Society*, *91*(8), 1015–1058. <https://doi.org/10.1175/2010BAMS3001.1>
- Schirber, S., Manzini, E., & Alexander, M. J. (2014). A convection-based gravity wave parameterization in a general circulation model: Implementation and improvements on the QBO. *Journal of Advances in Modeling Earth Systems*, *6*, 264–279. <https://doi.org/10.1002/2013MS000286>
- Simpson, J., Kummerow, C., Tao, W.-K., & Adler, R. F. (1996). On the tropical rainfall measuring mission (TRMM). *Meteorology and Atmospheric Physics*, *60*, 19–36. <https://doi.org/10.1007/BF01029783>
- Song, I.-S., & Chun, H.-Y. (2005). Momentum flux spectrum of convectively forced internal gravity waves and its application to gravity wave drag parameterization. Part I: Theory. *Journal of the Atmospheric Sciences*, *62*(1), 107–124. <https://doi.org/10.1175/JAS-3363.1>
- Song, I.-S., Chun, H.-Y., Garcia, R. R., & Boville, B. A. (2007). Momentum flux spectrum of convectively forced internal gravity waves and its application to gravity wave drag parameterization. Part II: Impacts in a GCM (WACCM). *Journal of the Atmospheric Sciences*, *64*(7), 2286–2308. <https://doi.org/10.1175/JAS3954.1>
- Stephan, C., & Alexander, M. J. (2015). Realistic simulations of atmospheric gravity waves over the continental US using precipitation radar data. *Journal of Advances in Modeling Earth Systems*, *7*, 823–835. <https://doi.org/10.1002/2014MS000396>
- Takahashi, N., Hanado, H., Nakamura, K., Kanamaru, K., Nakagawa, K., Iguchi, T., et al. (2016). Overview of the end-of-mission observation experiments of precipitation radar onboard the tropical rainfall measuring mission satellite. *IEEE Transactions on Geoscience and Remote Sensing*, *54*(6), 3450–3459. <https://doi.org/10.1109/TGRS.2016.2518221>
- Tao, W.-K., Iguchi, T., & Lang, S. (2019). Expanding the Goddard CSH algorithm for GPM: New extratropical retrievals. *Journal of Applied Meteorology and Climatology*, *58*(5), 921–946. <https://doi.org/10.1175/JAMC-D-18-0215.1>
- Tao, W.-K., Lang, S., Simpson, J., & Adler, R. (1993). Retrieval algorithms for estimating the vertical profiles of latent heat release their applications for TRMM. *Journal of the Meteorological Society of Japan. Series II*, *71*(6), 685–700. https://doi.org/10.2151/jmsj1965.71.6_685
- Tao, W.-K., Simpson, J., Lang, S., McCumber, M., Adler, R., & Penc, R. (1990). An algorithm to estimate the heating budget from vertical hydrometeor profiles. *Journal of Applied Meteorology and Climatology*, *29*(12), 1232–1244. [https://doi.org/10.1175/1520-0450\(1990\)029<1232:aateth>2.0.co;2](https://doi.org/10.1175/1520-0450(1990)029<1232:aateth>2.0.co;2)
- Tost, H., Jöckel, P., & Lelieveld, J. (2006). Influence of different convection parameterizations in a GCM. *Atmospheric Chemistry and Physics*, *6*, 5475–5493. <https://doi.org/10.5194/acp-6-5475-2006>
- Trinh, Q. T., Kalisch, S., Preusse, P., Ern, M., Chun, H.-Y., Eckermann, S. D., et al. (2016). Tuning of a convective gravity wave source scheme based on HIRDLS observations. *Atmospheric Chemistry and Physics*, *16*, 7335–7356. <https://doi.org/10.5194/acp-16-7335-2016>
- Tropical Rainfall Measuring Mission (TRMM). (2019). GPM PR and TMI on TRMM Combined Gridded Orbital Convective-Stratiform Latent Heating Profiles L3 1.5 hr 0.25° × 0.25° V06 [Dataset]. Goddard Earth Sciences Data and Information Services Center (GES DISC). <https://doi.org/10.5067/GPM/PRTMI/TRMM/CSH/3G/06>
- Yokoyama, C., Zipsper, E. J., & Liu, C. (2014). TRMM-observed shallow vs. deep convection in the eastern Pacific related to large-scale circulations in reanalysis data sets. *Journal of Climate*, *27*(14), 5575–5592. <https://doi.org/10.1175/JCLI-D-13-00315.1>